The Astrophysical Journal, 978:37 (32pp), 2025 January 01 https://doi.org/10.3847/1538-4357/ad8b45

Bar Formation and Destruction in the FIRE-2 Simulations

Sioree Ansar[1,2,3], Sarah Pearson[4,5,11], Robyn E. Sanderson[1,6], Arpit Arora[6], Philip F. Hopkins[7], Andrew Wetzel[8], Emily C. Cunningham[1,9,11], and Jamie Quinn[10]
[1] Center for Computational Astrophysics, Flatiron Institute, 162 5th Avenue, 21st Street, New York City, NY 10010, USA; sioreeansar@gmail.com
[2] Indian Institute of Astrophysics, 2nd Block, Koramangala, Bangalore, Karnataka 560034, India
[3] Pondicherry University, R.V. Nagar, Kalapet 605014, Puducherry, India
[4] The Center for Cosmology and Particle Physics, New York University, 726 Broadway, New York, NY 10003, USA
[5] Niels Bohr International Academy & DARK, Niels Bohr Institute, University of Copenhagen, Blegdamsvej 17, 2100 Copenhagen, Denmark
[6] Department of Physics & Astronomy, University of Pennsylvania, 209 S 33rd Street, Philadelphia, PA 19104, USA
[7] TAPIR, Mailcode 350-17, California Institute of Technology, Pasadena, CA 91125, USA
[8] Department of Physics & Astronomy, University of California, Davis, CA 95616, USA
[9] Department of Astronomy, Columbia University, 550 West 120th Street, New York, NY 10027, USA
[10] Department of Physics, University of California, Merced, 5200 N. Lake Road, Merced, CA 95343, USA
Received 2023 September 29; revised 2024 October 22; accepted 2024 October 23; published 2024 December 24

Abstract

The physical mechanisms responsible for bar formation and destruction in galaxies remain a subject of debate. While we have gained valuable insight into how bars form and evolve from isolated idealized simulations, in the cosmological domain, galactic bars evolve in complex environments, with mergers and gas accretion events occurring in the presence of the turbulent interstellar medium with multiple star formation episodes, in addition to coupling with their host galaxies' dark matter halos. We investigate the bar formation in 13 Milky Way–mass galaxies from the Feedback in Realistic Environments (FIRE-2) cosmological zoom-in simulations. 8 of the 13 simulated galaxies form bars at some point during their history: three from tidal interactions and five from internal evolution of the disk. The bars in FIRE-2 are generally shorter than the corotation radius (mean bar radius $\sim$1.53 kpc), have a wide range of pattern speeds (36–97 km s^{-1} kpc^{-1}), and live for a wide range of dynamical times (2–160 bar rotations). We find that the bar formation in FIRE-2 galaxies is influenced by satellite interactions and the stellar-to-dark-matter mass ratio in the inner galaxy, but neither is a sufficient condition for bar formation. Bar formation is more likely to occur, with the bars formed being stronger and longer-lived, if the disks are kinematically cold; galaxies with high central gas fractions and/or vigorous star formation, on the other hand, tend to form weaker bars. In the case of the FIRE-2 galaxies, these properties combine to produce ellipsoidal bars with strengths $A_2/A_0 \sim 0.1$–0.2.

Unified Astronomy Thesaurus concepts: Hydrodynamical simulations (767); Galaxy bars (2364); Galaxy interactions (600); Dark matter (353)

1. Introduction

Bars are triaxial structures at the centers of galaxy disks that form through global disk instabilities. Stars in barred potentials follow elongated orbits. Studies using isolated galaxy simulations have explored different formation mechanisms in controlled simulations with fine-tuned initial conditions (W. H. Julian & A. Toomre 1966; F. Hohl 1971; J. P. Ostriker & P. J. E. Peebles 1973; J. A. Sellwood & A. Wilkinson 1993; J. A. Sellwood 2014). These studies have shown that bars can form during the isolated evolution of disk galaxies (D. A. Gadotti 2011; J. A. Sellwood 2014) and during encounters with other galaxies or satellite galaxies (M. Gerin et al. 1990; S. Ghosh et al. 2021). Some studies have also shown that bars can be destroyed and regenerated (M. K. Cavanagh et al. 2022). Recently, observations of bars using the James Webb Space Telescope have generated interest in bar formation at high redshifts ($z_r \sim 1$–4; Y. Guo et al. 2023, 2024; Z. A. Le Conte et al. 2024). Studies have provided insights into the formation of bars in thick disks, which may exhibit similar properties to disk galaxies observed at high redshifts (A. Klypin et al. 2009; M. Aumer & J. Binney 2017; J. Reddish et al. 2022; S. Ghosh et al. 2023).

Detailed studies of the bar in the Milky Way (MW) have played a crucial role in understanding its dynamics, formation, and evolution using voluminous new survey data (e.g., C. Wegg et al. 2015, 2019; J. Bovy et al. 2019; M. Lucey et al. 2023). Other studies estimate the MW bar pattern speed using action space (W. H. Trick et al. 2021; W. H. Trick 2022) and transverse velocities (J. L. Sanders et al. 2019), and D. Grion Filho et al. (2021) have studied high-resolution numerical simulations of galaxy interactions (analogous to the MW–Sagittarius dwarf galaxy system) that can result in bar formation. Bars are thought to play a major role in star formation (e.g., J. A. L. Aguerri 1999; K. L. Masters et al. 2011, 2012), the internal evolution of galaxies (e.g., D. A. Gadotti 2011; J. A. Sellwood 2014), and stellar and gas dynamics (K. Sheth et al. 2005; S. Khoperskov et al. 2018; W.-Y. Seo et al. 2019; E. L. Łokas 2020). The formation of bars during tidal interactions with satellite galaxies has been studied in detail using *N*-body simulations (M. Lang et al. 2014; E. L. Łokas et al. 2014, 2016, 2018) and in cosmological simulations (T. Zana et al. 2018a, 2018b). The bar–halo connection has been explored in detail using isolated galaxy

[11] Hubble Fellow.

evolution simulations (e.g., E. Athanassoula & A. Misiriotis 2002; E. Athanassoula 2002), where bars slow down through the transfer of angular momentum to dark matter (DM) halos and the rest of the disk in the host galaxy due to angular momentum exchange (V. P. Debattista & J. A. Sellwood 1998, 2000; E. Athanassoula et al. 2013). Multiple studies have highlighted the connection between the DM halo angular momentum, disk angular momentum, and bar structure (S. Ansar et al. 2023; A. B. Romeo et al. 2023).

However, bars in the Universe evolve in a complex environment: their host galaxies undergo satellite interactions, mergers, gas accretion, and star formation, while the bars simultaneously interact with the host's DM halo. Multiple cosmological simulations have studied bar properties (F. Fragkoudi et al. 2021; M. Roshan et al. 2021), their abundance (Y. Rosas-Guevara et al. 2022), bar formation pathways (D. Izquierdo-Villalba et al. 2022), and bar evolution (Y. Rosas-Guevara et al. 2022; F. Fragkoudi et al. 2024). D. Irodotou et al. (2022) have shown that bars grow stronger in the absence of active galactic nucleus (AGN) feedback due to the formation of disky bulges that lead to stronger bars in Auriga simulations (R. J. J. Grand et al. 2017). Galaxies also contain a multiphase, turbulent interstellar medium (ISM), which many studies of bar dynamics have not considered. Past studies have also shown that bars can direct material into the central supermassive black hole in a galaxy, coupling bar formation to black hole feedback (I. Shlosman et al. 1989; P. F. Hopkins & E. Quataert 2011; D. Anglés-Alcázar et al. 2021; E. González-Alfonso et al. 2021). All the above processes can simultaneously affect bar formation in cosmological simulations, making it difficult to disentangle the contribution of each phenomenon. Even after decades of studies, bar formation in the cosmological context is a subject of debate.

The properties of bars have recently been studied in both large-volume simulations like Illustris (M. Vogelsberger et al. 2014a, 2014b), IllustrisTNG (R. Weinberger et al. 2017; A. Pillepich et al. 2018), and EAGLE (J. Schaye et al. 2015), and in zoomed simulations like Auriga (R. J. J. Grand et al. 2017) and NIHAO (L. Wang et al. 2015). While the large boxes can produce a substantial number of galaxies with different morphologies, they are constrained in balancing mass and spatial resolution with computational time. Hence, their ability to resolve the detailed dynamics of bars is somewhat limited. Cosmological zoom simulations like Auriga (R. J. J. Grand et al. 2017, 2024), NIHAO (L. Wang et al. 2015), and Feedback in Realistic Environments (FIRE-2;[12] P. F. Hopkins et al. 2018) have moderately sized samples of galaxies in a narrow galaxy mass range, but can resolve the disk scale height, and some of these simulations have a multiphase ISM (FIRE-2 and NIHAO; X. Ma et al. 2017; S. Garrison-Kimmel et al. 2018; J. Gensior et al. 2023). Most importantly, they contain enough particles in the bar-forming region to resolve bar dynamics (M. D. Weinberg 1994; M. D. Weinberg & N. Katz 2007a, 2007b; J. Dubinski et al. 2009) and the coupling to gas and DM.

The zoomed cosmological simulations thus provide useful tests of how differences in bar properties are related to differences in the implementation of the physical processes that affect bar formation, which differ widely between simulation suites.

[12] http://fire.northwestern.edu

In this work, we look at the 13 high-resolution MW-mass galaxies from the FIRE-2 suite (P. F. Hopkins et al. 2018). We use the FIRE-2 simulations to determine how bars form and when and how bar formation fails. We investigate whether the FIRE-2 bars are transient or long-lived and whether the disk properties affect the bar formation process.

We first describe the FIRE-2 simulations and the sample of galaxies that we use in our study (Section 2). We then present the different methods we use to analyze the sample galaxies in Section 3. We present the results in Section 4, on the different mechanisms of bar formation in FIRE-2 galaxies and how bar formation is affected by the host disk and halo properties. We discuss our results in Section 5, and in Section 6 we summarize and discuss the major findings of this study.

2. The FIRE-2 Simulations

We use the set of 13 MW-mass galaxies in the FIRE-2 suite, all of which are run with the GIZMO code (P. F. Hopkins 2015, 2017). GIZMO implements a gravity solver (TREE +PM) with a Lagrangian meshless, finite-mass method for hydrodynamics with the FIRE-2 physics model (P. F. Hopkins et al. 2018). In this prescription, stellar feedback is determined and injected locally by following the evolution of the individual mono-age, mono-abundance stellar populations represented by each star particle, using the stellar evolution models from STARBURST99 (C. Leitherer et al. 1999) and the P. Kroupa (2001) initial mass function. The simulations evolve from a redshift $z_r \sim 100$ to $z_r = 0$. The galaxies form hierarchically, individually transitioning from an early phase of multiple interactions and large starburst events to well-settled disks (X. Ma et al. 2017; S. Yu et al. 2021; J. Gensior et al. 2023; A. B. Gurvich et al. 2023; P. F. Hopkins et al. 2023; F. McCluskey et al. 2024) with a variety of star formation histories.

FIRE-2 simulations account for multiple physical phenomena to implement stellar feedback: radiative heating and cooling with free–free photoionization/recombination, photoelectric, Compton effect, dust collision, and cosmic rays (CRs). FIRE-2 considers molecular, metal-line, and fine-structure processes by tracking 11 different species separately. Star formation is implemented in self-gravitating, Jeans-unstable molecular gas that is self-shielding (following P. F. Hopkins et al. 2013) and has number density $n > 1000\,\mathrm{cm}^{-3}$. The FIRE simulations are able to produce disk galaxies with masses, scale radii, and scale heights that are comparable to observed MW-mass galaxies (X. Ma et al. 2017; S. Garrison-Kimmel et al. 2018; R. E. Sanderson et al. 2020; S. Yu et al. 2021; J. Gensior et al. 2023; A. B. Gurvich et al. 2023) and also realistic Giant Molecular Cloud populations (D. Guszejnov et al. 2020; S. M. Benincasa et al. 2020). Importantly for this study, the kinematic "coldness" of the stellar and gas disks of FIRE-2 galaxies has recently been shown by F. McCluskey et al. (2024) to be consistent with observed galaxies, agreeing well with the measurements of M31, M33, and galaxies from the PHANGS survey (J. Sun et al. 2020; I. Pessa et al. 2023), with the MW being somewhat kinematically cold relative to this population. The FIRE-2 model does not include feedback from black hole accretion.

The merger history of halos provides important information about the satellite interactions that can have a high tidal impact on the disk and lead to bar formation. The ROCKSTAR code (P. S. Behroozi et al. 2013a) is used on each of the simulation

Table 1
Summary of $z_r \sim 0$ Properties of the FIRE-2 MW-mass Galaxies Used in This Study

Simulation	$M_{\star,90}$ ($M_\odot$)	M_{200} ($M_\odot$)	R_{90} (kpc)	$V_{\rm max}$ (km s^{-1})	$R_{\rm max}$ (kpc)	References
(1)	(2)	(3)	(4)	(5)	(6)	(7)
m12r	1.3×10^{10}	1.10×10^{12}	10.4	147	9.8	(S20)
Louise	2.3×10^{10}	1.15×10^{12}	11.2	182	9.8	(G19a)
Juliet	3.3×10^{10}	1.10×10^{12}	8.1	209	1.4	(G19a)
Remus	4.0×10^{10}	1.22×10^{12}	11.0	298	1.5	(G19b)
m12w	4.8×10^{10}	1.08×10^{12}	7.3	247	3.2	(S20)
m12c	5.1×10^{10}	1.35×10^{12}	9.1	241	3.2	(G19a)
m12i	5.5×10^{10}	1.18×10^{12}	8.5	265	2.0	(W16)
Romeo	5.9×10^{10}	1.32×10^{12}	12.4	255	3.4	(G19a)
Thelma	6.3×10^{10}	1.43×10^{12}	11.2	237	6.6	(G19a)
m12f	6.9×10^{10}	1.71×10^{12}	11.8	276	2.2	(G17)
m12b	7.3×10^{10}	1.43×10^{12}	9.0	316	1.8	(G19a)
Romulus	8.0×10^{10}	2.08×10^{12}	12.9	299	1.5	(G19b)
m12m	1.0×10^{11}	1.58×10^{12}	11.6	284	7.1	(H18)

Note. Column (1): simulation name. Column (2): $M_{\star,90}$—stellar mass within a cylindrical radius ($R = \sqrt{x^2 + y^2}$) that encloses 90% of the stellar mass within $R = 20$ kpc and $|z| < 2$ kpc (I. B. Santistevan et al. 2020). Column (3): M_{200}—total mass of the DM halo within the spherical radius $r = R_{200}$ ($r = \sqrt{x^2 + y^2 + z^2}$), inside which the mean density is 200 times the matter density of the Universe. Column (4): R_{90}—radius that encloses 90% of the stellar mass within $R = 20$ kpc and $|z| < 2$ kpc (I. B. Santistevan et al. 2020). Column (5): $V_{\rm max}$—maximum circular velocity. Column (6): $R_{\rm max}$—spherical radius corresponding to the maximum circular velocity. Column (7): references—S20: J. Samuel et al. (2020); G19a: S. Garrison-Kimmel et al. (2019a); G19b: S. Garrison-Kimmel et al. (2019b); W16: A. R. Wetzel et al. (2016); G17: S. Garrison-Kimmel et al. (2017); and H18: P. F. Hopkins et al. (2018). For more details of the individual simulations, see A. Wetzel et al. (2023).

runs to generate halo catalogs. To study the evolution of the identified halos in each of the simulation snapshots, the code Consistent Trees (P. S. Behroozi et al. 2013b) was used to link the subhalos over time for each of the snapshots, to form a merger tree. The stars inside the virial radius of each of the DM halos, having velocities less than twice the halo circular velocity in the simulations, are identified and linked with the respective halos.

In this work, we specifically study 13 galaxies in FIRE-2 (see Table 1) having present-day mass similar to the MW, $M_{200} = 1$–$2 \times 10^{12}\ M_\odot$, seven of which are isolated hosts (no large neighbor within 10 Mpc) and six of which are in systems analogous to the MW–M31 pair. The initial mass of the gas particles is 7100 $M_\odot$ in the isolated systems and 3500 $M_\odot$ in the paired systems; star particles inherit the gas particle mass, which then decreases due to stellar evolution, leading to a typical star particle mass of 2000–5000 $M_\odot$ at late times. The stellar and DM softening lengths are fixed, based on the typical interparticle spacing, and the gas particles have an adaptive softening length (minimum of 1 pc; P. F. Hopkins et al. 2018). The simulation snapshots are saved at a frame rate of $\Delta t \sim 25$ Myr between snapshots for most of the simulation and with $\Delta t = 2.2$ Myr for the last 22 Myr before $z_r = 0$. We use gizmo_analysis (A. Wetzel & S. Garrison-Kimmel 2020a) and halo_analysis (A. Wetzel & S. Garrison-Kimmel 2020b) for post-processing of the simulation data.

We investigate whether the FIRE-2 galaxies form bars from about $z_r \sim 2$ onward, after the galaxies have settled into a disk (i.e., when the majority of disk particles have more kinetic energy in circular motion compared to random motion; see S. Garrison-Kimmel et al. 2018). One of the galaxies in this simulation suite (m12m) has been studied in detail by V. P. Debattista et al. (2019), where the authors have found a bar that transforms into an X-shaped bulge at the end of evolution (more details are given in Section 3.1).

In the early phase of evolution, galaxy interactions are frequent and the host galaxy is mostly dispersion-dominated. Each of the disks becomes rotation-dominated at a slightly different epoch, as studied in detail by A. B. Gurvich et al. (2023), F. McCluskey et al. (2024), and P. F. Hopkins et al. (2023). In general, the FIRE-2 galaxies are slightly more dispersion-dominated than MW estimates at $z_r = 0$, but not more so than the general population of MW-mass galaxies (S. Garrison-Kimmel et al. 2018; F. McCluskey et al. 2024).

In Figure 1, we present the total circular velocity curves of the galaxies in our sample within a radius of 10 kpc at $z_r = 0$. Most galaxies in the sample have similar mass distributions in the central region, except m12r and Louise, which have significantly smaller total stellar mass than the others. The circular velocity $V_{c,i}(r)$ at radius r is defined by taking into account the mass of the ith component (stars, gas, or DM) in the galaxy:

$$V_{c,i}(r) = \sqrt{\frac{GM_i(r)}{r}}. \quad (1)$$

The total circular velocity curve is due to the combined mass of all components. The maximum rotation velocity lies in the range $140 < V_{max}/(\mathrm{km\ s^{-1}}) < 320$ and the corresponding radius range is $1.4 < R_{\rm max}/(\mathrm{kpc}) < 9.8$ (see Table 1).

3. Detecting and Characterizing Bars in FIRE-2

In this section, we first describe how we determine whether the galaxies in the FIRE-2 simulations from Table 1 develop bars during any time of evolution. We then estimate the different bar characteristics for all the galaxies and present the features of these bars.

3.1. The Strength of FIRE-2 Bars

We search each galaxy in Table 1 for bar-like features from $z_r \sim 2$ to the present day, by calculating the mass-weighted bar

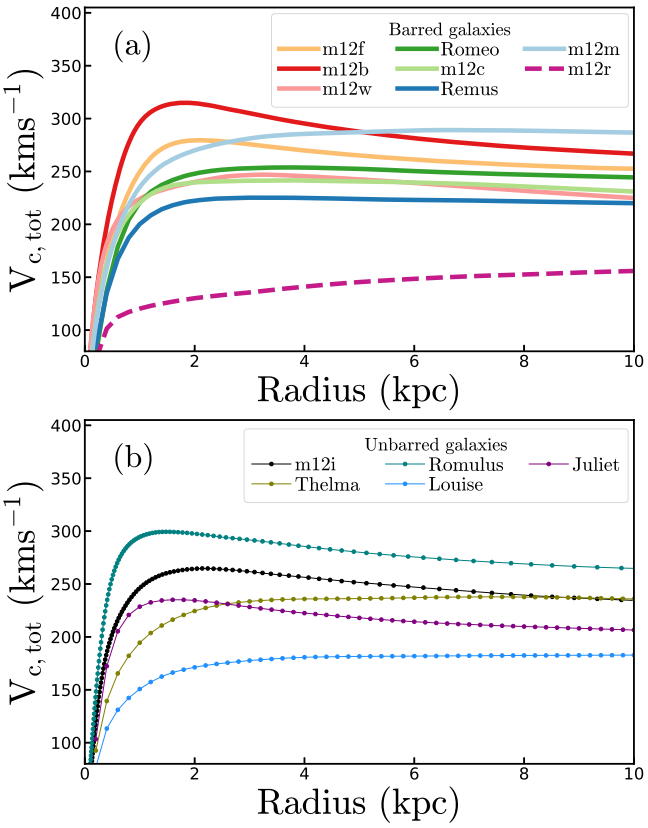

Figure 1. Circular velocity of all the FIRE-2 galaxies in Table 1 at $z_r = 0$. Panel (a): the colored thick lines show the galaxies that form bars (some of them do not survive until $z_r = 0$), and the dashed thick line is for m12r, which has low mass compared to the rest of the galaxies in this sample. Panel (b): the colored thin lines with circular marks show the unbarred galaxies. We use the above choice of color and line style for the simulations throughout the article.

strength as a function of radius in the plane of the stellar disk. The bar strength is defined as the maximum amplitude of the $m = 2$ Fourier mode of the 2D decomposition of the face-on stellar surface density distribution of the galaxy (E. Athanassoula & A. Misiriotis 2002; E. Athanassoula et al. 2013):

$$\frac{A_2}{A_0} = \left(\frac{\sqrt{a_2^2 + b_2^2}}{\Sigma_{i=1}^{N} m_{\star i}} \right), \tag{2}$$

where, in general for the mth mode, $a_m = \Sigma_{i=1}^{N} m_{\star i} \cos(m\theta_i)$, $b_m = \Sigma_{i=1}^{N} m_{\star i} \sin(m\theta_i)$, θ_i is the azimuthal coordinate, and $m_{\star i}$ is the mass of ith stellar particle.

We calculate the bar strength from the star particles as follows. First, we define and rotate into a coordinate system in which the z-direction is perpendicular to the "disk plane," defined by computing the principal axis system from the youngest 25% of star particles among the ones constituting the 90% mass within a 10 kpc radius and using the z-direction as the eigenvector corresponding to the smallest eigenvalue. Then we select stars in the disk: within 10 kpc of the galaxy center in $R \equiv \sqrt{x^2 + y^2}$ and within 2 kpc of the midplane in z. We then divide the disk into annuli of width $\Delta R = 50$ pc[13] and calculate A_2/A_0 by applying Equation (2) to the star particles in each annulus. We repeat this calculation in each snapshot of each simulation from $z_r = 2$ to the present day.

This measurement of bar strength has two limitations. First, it captures not only the bar but also any other asymmetric features in the disk that have approximate $m = 2$ symmetry, including spiral arms or remnants of galaxy mergers. Thus, we also require that the phase angle of the $m = 2$ Fourier mode,

$$\phi_2 = \tan^{-1}(b_2/a_2)/2, \tag{3}$$

be nearly constant over the length of the bar, which should rotate like a rigid object. Second, since our measure is mass-weighted, it is not directly comparable to the light-weighted bar strength measure calculated similarly from images. However, in this work, we are primarily interested in the mechanisms governing bar formation, for which the mass-weighted version is appropriate.

In Figure 2, we present face-on "images" of the central 4×4 kpc region of each of the 13 FIRE-2 galaxies at the time of their maximum bar strength $A_2/A_0|_{\rm max}$. Each panel also shows the time $t_{\rm max}$ of maximum bar strength for that galaxy in gigayears. The bar strength profile of each galaxy at $t_{\rm max}^{\rm lbt}$ is shown in panel (a) of Figure 3. m12f has the highest bar strength of $A_2/A_0|_{\rm max} = 0.203$, while Juliet shows the lowest peak bar strength $(A_2/A_0)_{\rm max} = 0.038$. We find bar strengths $\gtrsim$0.1 in 10 of the 13 galaxies.

In a different simulation run of m12m, the bar has an X shape in the younger population of stars, as studied previously by V. P. Debattista et al. (2019), where the bar is of higher strength ($A_2/A_0|_{\rm max} \sim 0.18$). However we find a maximum bar strength of $(A_2/A_0)_{\rm max} \sim 0.11$ for the version of m12m in this article. These two runs include slightly different physics prescriptions: the run analyzed here includes an implementation of turbulent metal diffusion in the gas phase, while the one analyzed in V. P. Debattista et al. (2019) does not. We do not expect this difference to have a direct effect on bar formation; however, any variation of the physics model will affect the star formation history of the galaxy, which varies stochastically between runs due to the randomness involved in triggering supernovae (P. F. Hopkins et al. 2018), and will therefore result in a slightly different evolution. We therefore attribute this difference to variations in the star formation and feedback histories between the runs. This degree of variation underlines from a theoretical standpoint the relatively arbitrary use of a cutoff value of A_2/A_0, especially since we see continuous variations in this measure with both time (as we will discuss in Section 3.2) and radius (Figure 3) in all our simulations.

One notable characteristic of the bars in Figure 2 is that their isodensity contours appear more rounded and less rectangular in shape, as compared to the more rectangular bars commonly seen in N-body simulations and some observations. As we will argue in Section 4.2.1, this is because the circular velocity curves of the DM component in the FIRE-2 barred galaxies are slow-rising, similar to the model in E. Athanassoula & A. Misiriotis (2002).

According to the most commonly used definition of a bar, $(A_2/A_0)_{\rm max} > 0.2$, none of the FIRE-2 systems would be considered to host a bar. However, this criterion was developed using light-weighted bar strengths calculated from images rather than the mass-weighted version that we calculate, making the value of this cutoff somewhat arbitrary. Furthermore, even for bar strengths below this nominal cutoff, we observe long-lived features in our simulations with $m = 2$

[13] Even with a larger bin size of 100–200 pc, the barred structures in the $m = 2$ component persist.

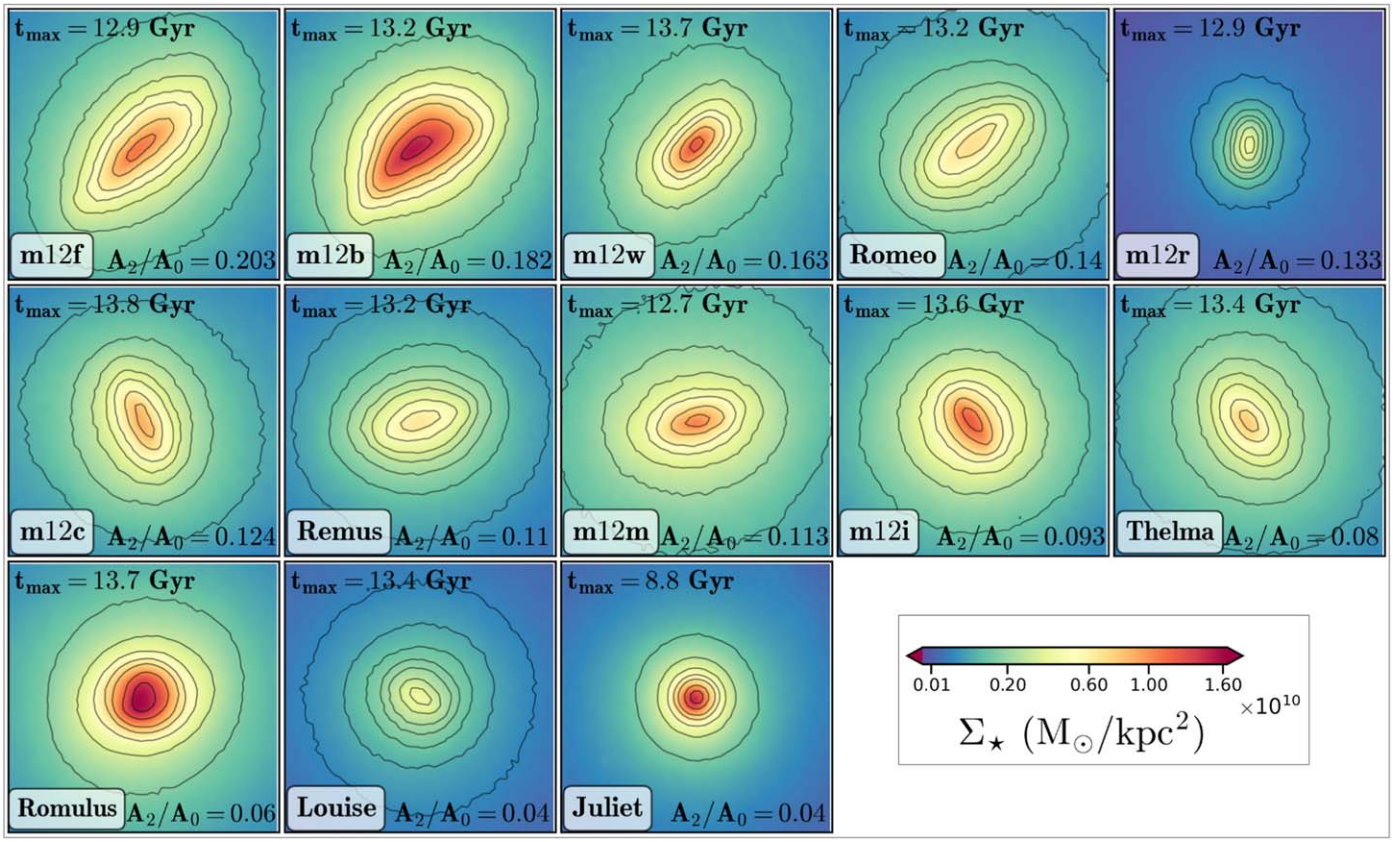

Figure 2. Bars in MW-mass galaxies from the FIRE-2 suite. The face-on projected stellar mass density for all star particles in the central (4 kpc)^3 volume is shown in each panel at the time of maximum bar strength A_2/A_0, with the high-density regions in each case scaled to red, the medium-density regions to yellow, and the low-density regions to blue, following the color bar of the stellar surface density $\Sigma_\star$ ($M_\odot$ kpc^{-2}). The contours are at 90%, 70%, 50%, 40%, 30%, 20%, and 10% of the peak density in each galaxy. The value of the bar strength and the time in gigayears are provided in each panel. The bars and bar-like structures show a variety of shapes and sizes; for example, m12b (top row, second panel from right) is lopsided (see E. L. Łokas 2021 for more examples of lopsided bars), and m12w (top row, middle panel) is distinctly rectangular. Some galaxies (e.g., Juliet, Louise, and Romulus) do not show bars according to our definition (Section 3.1).

symmetry in the inner galaxy. Therefore, we instead use the following operational criteria to define a bar:

1. For an asymmetry to be called a bar, the instantaneous peak bar strength at any radius should be $(A_2/A_0)_{max} > 0.1$ for at least $1.5T_o$, where T_o is the orbital time $2\pi r/V_c(r)$ at the outer edge of the bar.
2. The bar position angle (PA) ϕ_2 (Equation (3)) should be constant within $\pm 5°$ over the entire bar length (Figure 3, panel (c)).

Figure 3, panel (a) shows the bar strength as a function of cylindrical radius R in the disk plane for all 13 FIRE-2 galaxies at the time of their peak bar strength. All the galaxies having bar strength $A_2/A_0 > 0.1$ in panel (a) are candidate bars, some of which we confirm in Section 3.2 after measuring their duration. In panel (b), we show the bar strength profiles of confirmed bars (i.e., those lasting longer than $1.5T_o$) as a function of R scaled by the bar corotation radius (Section 3.5). The bar in m12r is missing from panel (b), as we cannot measure the pattern speed and consequently the corotation of its extremely short bar (more details are given in Section 3.4). In panel (c), we show the variation of the mean-subtracted PA $\phi_2 - \langle\phi_2\rangle$ as a function of R scaled by the bar radius a_s (Section 3.3). Here, $\langle\phi_2\rangle$ is the mean of phase ϕ_2 around the radius of the peak bar strength. The PA of each barred galaxy is constant within $\pm 5°$ over the bar's length ($R/a_s < 1$).

Figures 2 and 3 show that with our criteria, eight of the FIRE-2 galaxies have bars: m12f, m12b, m12m, m12w, Remus, Romeo, m12c, and m12r. Some other galaxies, such as m12i and Thelma, have asymmetries that maintain a constant PA but have $A_2/A_0 < 0.1$ throughout their evolution. The rest of the galaxies (Louise, Juliet, and Romulus) do not satisfy either criterion; nor could we identify a bar-like structure in these galaxies through visual inspection of their stellar disks throughout their evolution. Instead, we see a bulge-like stellar distribution at the centers of Louise, Juliet, and Romulus (see Figure 2).

3.2. Bar Duration

We next determine the duration over which each bar has $(A_2/A_0)_{max} > 0.1$ and constant phase ϕ_2. Figure 4 gives an example of the evolution of these quantities with time for two of the strongest bars, m12f (top panel) and m12b (bottom panel). Both bars undergo episodes of varying length, where $A_2/A_0 > 0.1$ (blue shaded regions) and constant bar phase ϕ_2 (pink shaded regions).

Generically, we define any time interval with bar strength $(A_2/A_0)_{max} > 0.1$ and constant bar PA to be a "bar episode." However, the full picture is slightly more complex, as illustrated by the examples shown in Figure 4. In m12f (panel (a)), there is an early bar episode from $t = 9.86$ to 10.04 Gyr, followed by a long interval where $(A_2/A_0)_{max} > 0.1$

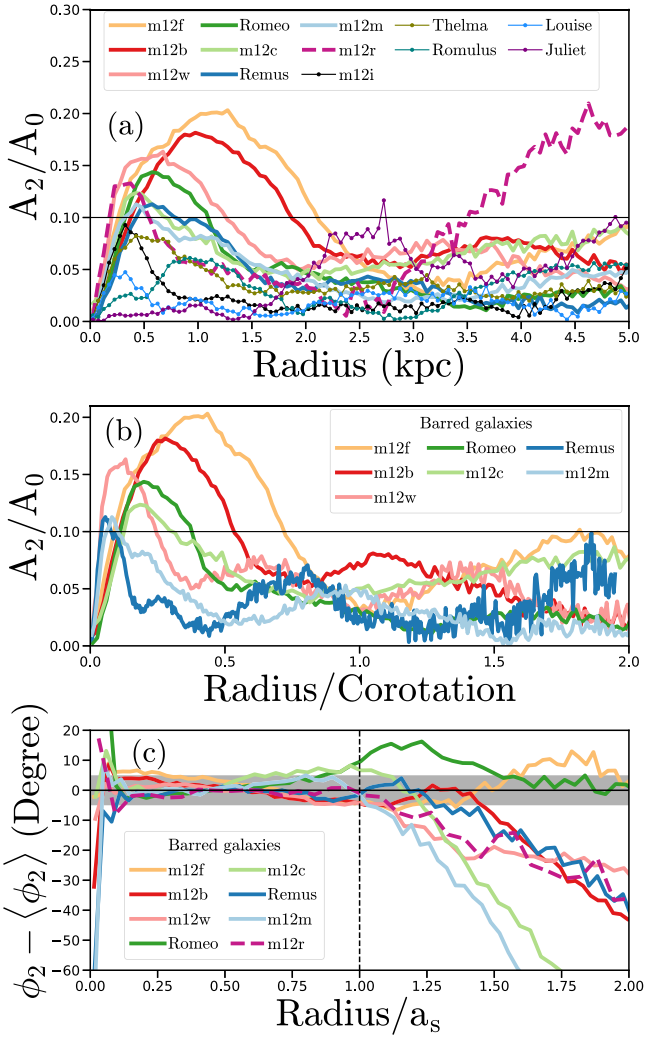

Figure 3. Bar profiles. Panel (a) shows A_2/A_0 profiles as a function of disk radius for all the galaxies, both barred (thick lines) and unbarred (dotted thin lines), at the time of peak bar strength (see Figure 2). Panel (b) shows only the barred galaxy profiles as a function of disk radius, scaled by the bar corotation radius. For all the barred galaxies, the peak A_2/A_0 is well inside corotation. We do not add m12r in panel (b), as we cannot measure its pattern speed to determine its corotation radius (Section 3.4). Panel (c) shows the mean-subtracted phase angle $\phi_2 - \langle\phi_2\rangle$ as a function of disk radius, scaled by the bar radius (a_s), where the mean is over the five data points around ϕ_2 at the radius of the peak A_2/A_0. The bar phase ϕ_2 must be within $0° \pm 5°$ (shaded) to maintain the nearly constant PA characteristic of a bar. Within the bar length (black dashed vertical line), the PA is nearly constant for all the barred galaxies, except in the very central region, where the bar strength drops below $A_2/A_0 < 0.1$.

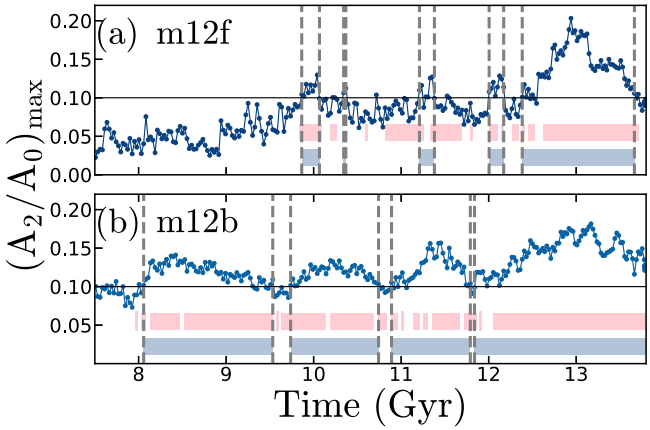

Figure 4. Bar duration in m12f (panel (a)) and m12b (panel (b)). This figure shows the evolution of maximum bar strength within a radius of 2 kpc, $A_2/A_{0,(r<2\,kpc)}$, of two FIRE-2 galaxies m12f and m12b (having the strongest bars) with time (in gigayears). When the bar strength $(A_2/A_0)_{max} > 0.1$ (blue shaded regions bounded by dashed vertical lines) for a time interval $\Delta t > T_o$ (as per our bar definition), and also when the bar PA is nearly constant (pink shaded regions; for details of the PA see Section 3.1), we call it a bar episode (overlapping time intervals of blue and pink shades). For m12f, there are two major bar episodes: (1) $t = 9.86$–10.04 Gyr and (2) $t > 12.38$ Gyr. For m12b, the bar episode is from $t = 8.05$ to 13.8 Gyr (∼5.7 Gyr), as there is more uniform overlap between the high bar strength (blue shaded region) and constant bar phase ϕ_2 (pink shaded region) for 5.7 Gyr. For more details of bar episodes see Section 3.2.

Table 2
Bar Duration Estimates

Simulation	Duration T_d (Gyr)	Orbital time T_o $\frac{2\pi r}{V_c(r)}$ (Gyr)	$\frac{T_d}{T_o}$
(1)	(2)	(3)	(4)
m12f (episode 1)	0.18	0.024	7.4
m12f (episode 2)	1.28	0.041	31.2
m12b	5.74	0.035	163.5
Romeo	0.77	0.034	22.6
Remus	0.79	0.035	22.4
m12w	0.13	0.037	3.5
m12m	0.069	0.04	1.73
m12c	0.066	0.037	1.78
m12r	0.39	0.052	7.6

Note. Column (1): simulation name. Column (2): duration T_d for a single bar episode, according to the criteria in Section 3.1 (m12f has two bar episodes). Column (3): orbital time $T_o = 2\pi r/V_c(r)$ estimated at the edge of the bar, $r = a_s$ (see Section 3.1 and Appendix B). Column (4): number of times the bar rotates during its duration.

occasionally but ϕ_2 is not constant. Then the bar strength again rises to $(A_2/A_0)_{max} > 0.1$ for $t > 12.38$ Gyr with constant ϕ_2, and remains stable for a second bar episode of ∼1 Gyr. The bar-like asymmetry in m12f does not satisfy both bar criteria between 10.04 and 12.38 Gyr; hence, we consider m12f to have two bar episodes of durations 0.18 and 1 Gyr, separated by an unbarred period of 2.3 Gyr. On the other hand, in m12b (panel (b)), the bar strength dips below 0.1 for several very short intervals (0.20 Gyr, 0.148 Gyr, and 0.048 Gyr), while the bar phase ϕ_2 is almost continuously constant from $t = 8.05$ to 13.8 Gyr. We consider this to be one continuous bar episode with a duration of nearly 5.7 Gyr.

Our distinction between bar episodes is somewhat sensitive to the lower bound on $(A_2/A_0)_{max}$. If we choose a minimum strength of 0.08 instead of 0.1, there would be more bar episodes for m12f according to our bar criteria. This is a limitation of our bar definition criteria and similar choices in the literature, as the choice of this lower limit on bar strength is largely empirical. Additionally, we note that the number of bar rotations is sensitive to the radius at which we estimate orbital time T_o. We evaluate T_o at the edge of the bar that varies with evolution (see Appendix B).

All other galaxies in our simulation suite (m12m, Romeo, Remus, m12w, m12c, and m12r) undergo a single episode of high bar strength that ends when the bar strength either decreases below $A_2/A_0 < 0.1$ (m12m, Romeo, and m12r) or remains high ($A_2/A_0 \gtrsim 0.1$) until the end of the galaxy's

Table 3
Bar Characteristics

Name	$\left(\frac{A_2}{A_0}\right)_{\rm max}$	$T_{\rm peak}$ (Gyr)	$z_{r,\rm peak}$	$\Omega_{p,\ \rm D}$ (km s^{-1} kpc^{-1})	$\langle\Omega_{p,\ \rm TW}\rangle$ (km s^{-1} kpc^{-1})	$\Delta z_r\vert_{\rm TW}$	$\Omega_{p,\ \rm peak}$ (km s^{-1} kpc^{-1})	$R_{\rm co}$ (kpc)	a_s (kpc)	$\mathcal{R}$	$Q_{\star,\rm min}$
(1)	(2)	(3)	(4)	(5)	(6)	(7)	(8)	(9)	(10)	(11)	(12)
Disks with bars: $A_2/A_0 > 0.1$											
m12f	0.203	12.94	0.064	73.9	70.50	0.07–0.05	91.07	2.93	1.86	1.67	0.94
m12b	0.182	13.17	0.046	89.5	85.37	0.0016–0.0	81.6	3.5	1.79	1.95	0.87
m12b	0.182	13.17	0.046	89.5	84.23	0.055–0.036	81.6	3.5	1.79	1.95	0.87
m12w	0.163	13.79	0.0	46.8	⋯	⋯	⋯	5.17	1.35	3.82	1.08
Romeo	0.144	13.28	0.038	⋯	69.37	0.055–0.023	82.9	2.9	1.32	2.19	1.07
m12r	0.133	12.98	0.061	⋯	⋯	⋯	⋯	⋯	0.81	⋯	1.06
m12c	0.123	13.77	0.001	67.0	⋯	⋯	97.4	2.3	1.27	1.81	0.97
Remus	0.113	13.21	0.041	93.8	42.81	0.048–0.034	36.09	10.25	1.58	6.48	1.72
m12m	0.112	12.68	0.084	⋯	⋯	⋯	49.5	5.3	1.53	3.59	1.14
Disks with $A_2/A_0 < 0.1$											
m12i	0.092	13.62	0.013	90.19	⋯	⋯	⋯	⋯	0.7	⋯	0.99
Thelma	0.082	13.46	0.024	57.50	⋯	⋯	⋯	⋯	1.0	⋯	1.18

Note. Column (1): simulation name. Column (2): peak bar strength overall times. Column (3): time of peak bar strength. Column (4): redshift of peak bar strength. Column (5): bar pattern speed measured directly from high-cadence snapshots ($0.0016 < z_r < 0.0$). Column (6): median bar pattern speed measured using the TW method. Column (7): range of redshifts used for the TW method. Column (8): TW pattern speed at peak bar strength (for more details, see Appendix D). Column (9): $R_{\rm co}$—corotation radius at peak bar strength. Column (10): a_s—bar semimajor axis length (bar radius) at peak bar strength. Column (11): $\mathcal{R} = R_{\rm co}/a_s$ at peak bar strength. Column (12): minimum $Q_\star$ within 5 kpc (see Section 3.6) at peak bar strength. The missing values of $\Omega_{p,\ \rm D}$ (Column (5)) indicate the bar does not exist at the end of the simulation and there is no constant pattern speed in the bar region. The missing values in Columns (6), (7), (8), (9), and (11) mean that we cannot measure these quantities, as the bars are weak and short in length. We could measure the TW pattern speeds for the two episodes in m12b (see columns (6) and (7) for m12b) and both episodes have all other quantities the same for the rest of the columns ((1)–(5) and (8)–(12).

evolution (until ∼13.8 Gyr for m12w, Remus, and m12c). We list the durations of the bar episodes for all the galaxies in Table 2.

Using the criteria for defining a bar in Section 3.1, eight of the 13 FIRE-2 galaxies have bars at some point in their evolution: m12f, m12b, Remus, Romeo, m12w, m12m, m12c, and m12r. The other five never reach the $A_2/A_0 > 0.1$ limit during their evolution: m12i, Thelma, Louise, Romulus, and Juliet.

3.3. Bar Length

We estimate the bar length from the face-on stellar density distribution (as shown in Figure 2) at the time of peak bar strength, using four different methods from the literature: (1) ellipse fitting of the bar region and bar PA measurement; (2) radial bar strength profile; (3) the difference between surface densities along the bar major and minor axes (E. Athanassoula & A. Misiriotis 2002; P. Erwin 2018); and (4) the bar and interbar density contrast (J. A. L. Aguerri et al. 2000). Each method gives a slightly different bar length, as discussed in Appendix A. See also L. Michel-Dansac & H. Wozniak (2006) and S. Ghosh & P. Di Matteo (2024) for discussions of different methods of measuring bar length. For the galaxies that have bars according to our definition, we report the semimajor axis length a_s (bar radius) averaged across all four methods in Table 3. The lengths measured by each of the individual methods are given in Table 5 of Appendix A.

3.4. Bar Pattern Speed

Except just before $z_r = 0$, the simulation snapshots are spaced too far apart to estimate the bar pattern speed Ω_p directly, by calculating the rate of change of the $m = 2$ mode Fourier phase angle ϕ_2 with time. Instead, we apply the Tremaine–Weinberg (TW) method (S. Tremaine & M. D. Weinberg 1984) to optimally projected 2D density maps of star particles older than 100 Myr,[14] following the method outlined in M. R. Merrifield & K. Kuijken (1995). Complete details of how we apply the TW method to the simulated bars are given in Appendix C.

To validate the TW method on our simulations, we compare the result with the pattern speed measured directly from the time derivative of the $m = 2$ Fourier phase angle, $\Omega_p = d\phi_2/dt$, in the four galaxies hosting a bar during the last 22 Myr of evolution, for which 10 snapshots are saved with a time interval of 2.2 Myr. We can compare the pattern speeds determined by both methods for m12b, m12c, and Remus. We find that estimates from both methods are consistent for bars with $A_2/A_0|_{\rm max} \gtrsim 0.1$ and $2a_s \gtrsim 2.5$ kpc.[15] Among our sample, this allows us to measure the pattern speed using the TW method with confidence for m12b, m12f, Romeo, and Remus. We can additionally get a direct measurement of the pattern speed at $z_r = 0$ for the bars in m12c, m12m, and m12w, for which the bars are too weak and short to apply TW. These values are listed in Table 3. We discuss the consistency of the TW method with direct measurements of the pattern speed in more detail in Appendix D.

We also find a match between the measurements of pattern speed from the TW method and from the code patternSpeed.py developed by W. Dehnen et al. (2023; see Appendix D). In one of the cases in m12b, we find a steady decrease in bar pattern speed, which for a fixed bar length and mass would

[14] The TW method is based on the continuity equation and is therefore applicable to a population of stars of the same age; as the stars in bar orbits are mostly old, we select stars older than 100 Myr.

[15] The TW method requires an inclined disk (∼45°) that shortens the apparent bar length by a factor $1/\sqrt{2}$.

indicate a loss of angular momentum (see Appendix E). However, as the bar in m12b evolves, it lengthens and accumulates more stars, which could compensate for a decrease in pattern speed to maintain the angular momentum. The change in bar angular momentum results from two opposing effects: the loss of angular momentum from the bar, which slows down its pattern speed, and the gain in angular momentum from adding stars in the bar orbits, which increases the bar's length. External torques from satellite galaxies can also impact the bar angular momentum. It is challenging to separate the effects of angular momentum changes among the bar, disk, satellites, and DM halo in a cosmologically evolving system.

3.5. Corotation

We calculate the corotation radius, $R_{\rm co}$, at which the circular speed in the disk plane, $\Omega(R)$, is equal to the pattern speed of the bar obtained in Section 3.4. To determine the circular speed $\Omega(R)$ as a function of cylindrical radius R, we use a composite potential model of each FIRE-2 galaxy, as described in A. Arora et al. (2022), for the appropriate snapshots of each simulation. In brief, the models are implemented using the Agama dynamics package (E. Vasiliev 2019), with a spherical harmonic basis expansion for the halo (DM and hot gas) and a cylindrical spline basis expansion for the disk (cold gas and stars). Both components are constrained to be axisymmetric, for consistency with the assumptions used to define $R_{\rm co}$. Using this smooth model, we calculate the derivative of the axisymmetric potential $\Phi(R,\ z)$ at the disk midplane to determine the circular speed:

$$\Omega(R) = \frac{1}{R}\frac{\partial \Phi(R,\ z)}{\partial R}\bigg|_{z=0}. \tag{4}$$

The radius at which $\Omega(r) = \Omega_p$ then gives the bar corotation radius $R_{\rm co}$, as presented in Table 3. All the bars are well within the corotation radius.

Using the bar length $2a_s$ and the corotation radius, we estimate the $\mathcal{R}$-parameter $\mathcal{R} \equiv R_{\rm co}/a_s$, also provided in Table 3. $\mathcal{R}$ is greater than 1.4 for all the bars. However, the pattern speeds we measure are not appreciably different from those measured for real systems: they lie between 36 and 97 km s^{-1} kpc^{-1} (Table 3). All the bars in FIRE-2 are shorter than their corotation radius, with $a_s < R_{\rm co}$ (see Table 3).

3.6. Disk Stability

Global disk instabilities like bars can form via swing amplification (W. H. Julian & A. Toomre 1966), a process that depends sensitively on the properties of the central regions of the disk. The tendency to swing amplification is usually quantified using one of several metrics, including the Toomre Q parameter, which compares the radial velocity dispersion of the disk stars to the mass surface density of a disk. Even though the Toomre Q parameter denotes instability against the $m = 0$ axisymmetric perturbation and not the $m = 2$ perturbations, a value of Q lower than 1 indicates that the disk is unstable to gravitational instabilities. While there are other methods for probing disk instability (J. P. Ostriker & P. J. E. Peebles 1973; G. Efstathiou et al. 1982; M. S. Fujii et al. 2018; O. F. Marioni et al. 2022), we find that they all generally yield results similar to those obtained using the Toomre Q parameter for weak bars. Therefore, we continue to use the well-established Toomre Q parameter to assess disk instability.

One of the necessary conditions for swing amplification is that $Q \gtrsim 1$, so that local overdensities have a chance to grow by swing amplification rather than gravitational instability, but not by so much that the random motion measured by $\sigma_{z,\star}$ excludes bar-supporting radial orbits. A. Toomre (1981) showed that $1 < Q < 2$ is necessary to form a bar in a Mestel disk.

To investigate whether this condition is still reflective of our cosmological bars, and to understand whether gas flows in the central galaxy can contribute to bar formation, we calculate Q for both the stellar disk and the gas disk of each simulated galaxy in our sample. We calculate $Q_\star$ for the stellar disk by modifying the expression in A. Toomre (1964) to include the gravity of the gas and DM:

$$Q_\star = \frac{\sigma_R \kappa}{3.36 G (\Sigma_\star + \Sigma_{\rm gas} + \Sigma_{\rm DM})}, \tag{5}$$

where σ_R is the stellar dispersion in the plane of the disk, κ is the epicyclic frequency ($\kappa^2(R) = \partial^2\Phi(R,\ z)/\partial^2 R|_{z\ =\ 0} + (3/R)\partial\Phi(R,\ z)/\partial R|_{z\ =\ 0}$; estimated using the potential model of each FIRE-2 galaxy presented in A. Arora et al. 2022, 2024; see Section 3.5), and $\Sigma_\star + \Sigma_{\rm gas} + \Sigma_{\rm DM}$ are the surface densities of stars, gas, and DM, respectively, within ± 0.5 kpc of the disk plane, as we intend to measure the local instability close to the midplane. The gas disk $Q_{\rm gas}$ is determined using an analogous expression from M. E. Orr et al. (2020):

$$Q_{\rm gas} = \frac{\sqrt{2}\,\sigma_z \Omega}{\pi G (\Sigma_{\rm gas} + \gamma \Sigma_\star)}, \tag{6}$$

where σ_z is the gas dispersion perpendicular to the disk plane, Ω is the circular speed, and γ is the fraction of the stellar component that lies within the gas disk scale height and therefore contributes to the self-gravity of the gas disk.

Although the disk instability criterion is based on the minimum value of Q, the Q-maps in Figure 5 show the regions that fall under this criterion at different times of evolution (M. E. Orr et al. 2020). We calculate $Q_\star$ and $Q_{\rm gas}$ for all barred galaxies in our sample in the central 10×10 kpc^2 region of the disk with $|z| \leqslant 0.5$ kpc. We evaluate the surface densities using face-on bins of 0.1×0.1 kpc^2 area. The mean $Q_{\rm gas}$ is in the range of $0.36 < \langle Q_{\rm gas} \rangle < 1.1$ in the inner 5 kpc of most of the galaxies' centers. We do not find a correlation between bar strength and $Q_{\rm gas}$, so we focus on $Q_\star$ in the rest of this section.

In Figure 5, we show the evolution of $Q_\star$ in the central region (10×10 kpc^2, $|z| < 0.5$ kpc) of the disk of each barred galaxy during bar formation. The first eight rows show the barred galaxies in descending order of bar strength, and the last row shows a typical example of an unbarred galaxy: Louise, which has $(A_2/A_0)_{\rm max} = 0.06$. The first column shows each disk in an unbarred phase ($A_2/A_0 << 0.1$). The second column shows the disk when the bar instability has begun to grow, but still $A_2/A_0 < 0.1$. The third column is when $A_2/A_0 \sim 0.1$ in each barred system, and the fourth column shows $Q_\star$ at the peak bar strength. At peak bar strength, we can easily trace the $1 < Q_\star < 2$ region (yellow and orange colors) associated with each bar. Extended spiral structures with nearly as low Q extend from each end of the bars in many cases, and the bars often show a two-lobed structure. These features all trace the combined high stellar and gas surface density ($\Sigma_\star + \Sigma_{\rm gas}$) from the denominator of Equation (5), showing that this factor plays

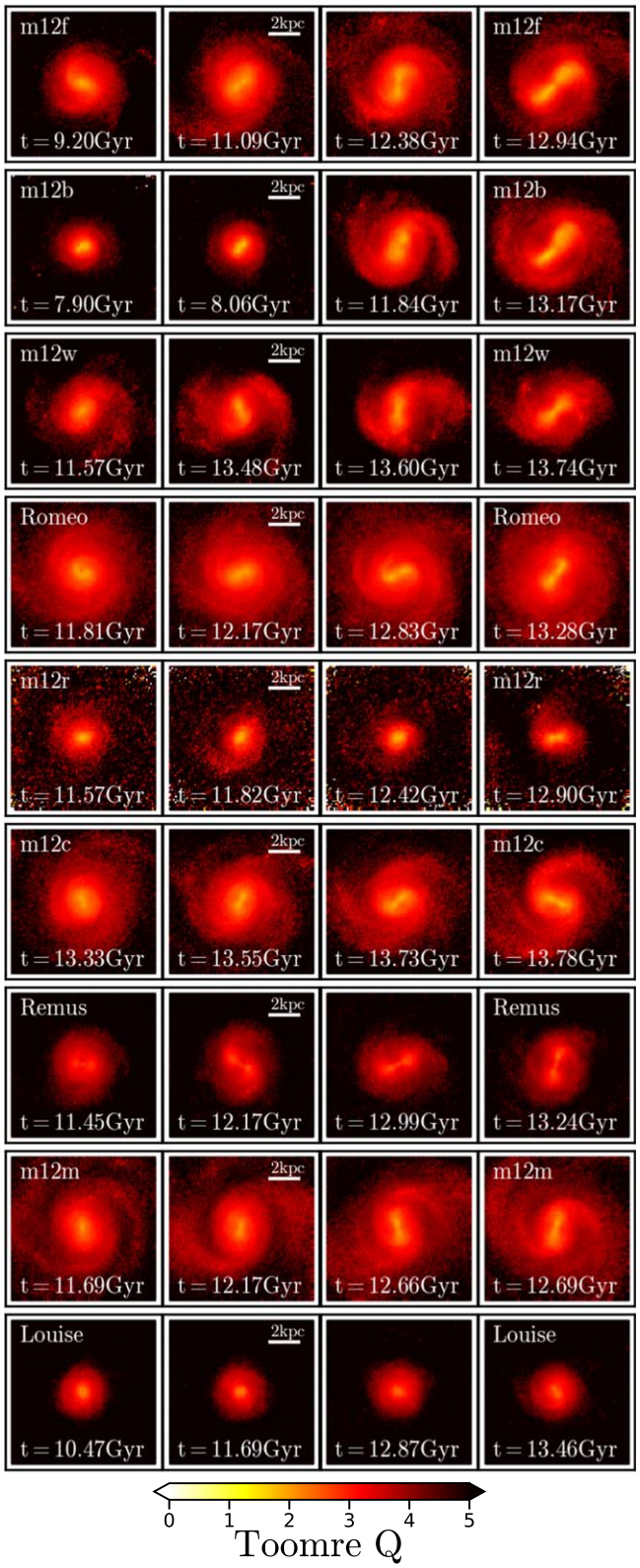

Figure 5. The evolution of $Q_\star$ during bar formation for the eight barred galaxies, in descending order of peak bar strength (rows 1–8), and a typical unbarred galaxy (Louise; row 9). The first column shows each system prior to bar formation; the second shows the onset of bar instability; the third shows when A_2/A_0 first exceeds 0.1; and the fourth shows the snapshot of peak bar strength.

the leading role in setting $Q_\star$. The other quantities in the equation that vary with position (σ_R, κ, and $\Sigma_{\rm DM}$) do not show any prominent features in their maps. Louise, the unbarred galaxy in the last row of Figure 5, looks very different from the barred galaxy maps, showing no features with low $Q_\star$.

Every galaxy in Figure 5 reaches its lowest $Q_\star$, close to 1.0, in the center of the galaxy at the time of peak bar strength. Table 3 lists these values. At larger R, $Q_\star$ gradually increases, creating a fairly large region where $Q_\star$ is high but not too high, appropriate for the growth of the bar by swing amplification. The typical $Q_\star$ in this region is between 2 and 3, rather than 1 and 2 as for the Mestel disk example, which is strikingly similar given the significant differences between the idealized case and our simulations.

We carried out several other tests to examine and quantify disk instability (J. P. Ostriker & P. J. E. Peebles 1973; G. Efstathiou et al. 1982; O. F. Marioni et al. 2022); also see Section 4.2.2), which lead to a similar conclusion. The FIRE-2 bars are weak in strength and have properties that lie in the boundary of strong and unbarred galaxies.

4. The Origins of FIRE-2 Bars

Bars can form during satellite interactions with galaxies and during internal evolution (D. A. Gadotti 2011; J. A. Sellwood 2014) in the disk under favorable conditions as the disk undergoes gravitational instabilities (F. Hohl 1971; J. P. Ostriker & P. J. E. Peebles 1973). A cold disk (J. P. Ostriker & P. J. E. Peebles 1973) with high surface density and low gas content, which is centrally baryon-dominated, favors bar formation. On the other hand, the presence of a centrally concentrated bulge or DM halo, which does not participate in the transfer of angular momentum from the disk to the DM halo, may make the disk stable against bar formation (J. P. Ostriker & P. J. E. Peebles 1973). However, previous studies have also shown that the distribution of DM (in live halos) in the central region of the disk affects the bar morphology by the transfer of angular momentum from the disk to the DM halo (F. Combes & R. H. Sanders 1981; E. Athanassoula 2002; E. Athanassoula & A. Misiriotis 2002), making the bar stronger and more rectangular for a disk dominated by DM.

In this section, we investigate how many of these phenomena affect bar formation and bar morphology in the FIRE-2 galaxies: satellite interactions (Section 4.1), internal evolution of the disk (Section 4.2), the relative concentration of different components in the central galaxy (Section 4.2.1), the kinematic coldness of the disk (Section 4.2.2), and the disk gas fraction (Section 4.2.3).

4.1. Bar Formation from Satellite Interactions

In this subsection, we investigate which FIRE-2 simulations likely had bar formation triggered by interactions with satellites.

I. D. Karachentsev & D. I. Makarov (1999) defined a tidal index, $\Theta = \log_{10}\left(\frac{M_{\rm sat}}{D_{\rm H}^3}\right)$, and used it to quantify the effects of satellites and minor mergers on the disks of host galaxies (see also D. R. Weisz et al. 2011; S. Pearson et al. 2016), where $M_{\rm sat}$ is the mass of the satellite (in units of $M_\odot$) and $D_{\rm H}$ is the distance of the satellite from the host galaxy's center (in kiloparsecs).

However, disks with different masses respond differently to satellite interactions. To compare the impacts of satellites on the various galaxies in FIRE-2, we need to consider how the properties of the host disks vary across the simulation suite. We

therefore define a scaled tidal index: $\Gamma = \log_{10}\left(\frac{M_{\rm sat}/M_{\rm host}}{(D_{\rm H}/R_{\rm H})^3}\right)$, where $R_{\rm H}$ is the effective radius of the host and $M_{\rm host}$ is the host galaxy's mass. The quantity $M_{\rm host}/R_{\rm H}^3$ can also be expressed in terms of the circular velocity V_c at a given radius R in the host galaxy, $M_{\rm host}/{R_{\rm H}}^3 = V_c^2/GR^2$, and measures the concentration of the host galaxy. We are interested in interactions close enough to the galaxy center to affect orbits on the rising part of the rotation curve (see Section 3.6), so we evaluate the quantity $M_{\rm host}/R_{\rm H}^3$ at the peak of the circular velocity curve:

$$\Gamma = \log_{10}\left(\frac{M_{\rm sat}/D_{\rm H}^3}{V_{c,\rm max}^2/GR_{\rm max}^2}\right), \quad (7)$$

where $V_{c,\rm max}$ is the maximum circular velocity and $R_{\rm max}$ is the corresponding radius (both these quantities are given in Table 1). In this expression, we take masses in units of $M_\odot$, distances in kiloparsecs, and speed in kilometers per second.

We search for the satellites that interact with the host disks in FIRE-2 simulations at different times during evolution by investigating the merger trees of the DM subhalos in each system. Merger trees are constructed using the codes ROCKSTAR (P. S. Behroozi et al. 2013a) and Consistent Trees (P. S. Behroozi et al. 2013b), which identify DM subhalos and trace their evolutionary history. We present the details of the steps we use for finding the satellites in Appendix F.

To compare the impacts of different satellites on bar formation in each of the FIRE-2 simulations, we first calculate Γ for each satellite in each of the FIRE-2 simulations as a function of time. Since $D_{\rm H}$ varies as a function of time, so will Γ, which reaches its maximal value when a satellite is at pericenter or during merger.

We select satellites for which $\Gamma > -2.45$ during at least one pericentric passage. This value for Γ is based on work by C. W. Purcell et al. (2011), who showed that a Sagittarius-like dwarf galaxy ($M_{\rm sat} = 10^{10.5}\ M_\odot$) at a pericenter of 30 kpc produced a pronounced bar in their isolated N-body simulations of an MW-like galaxy with $M_{\rm host} = 3.59 \times 10^{10}\ M_\odot$. We take $R_{\rm host} = R_{\rm eff} = 4.77$ kpc and use this to calculate Γ, since a rotation curve is not provided in the paper, from which we could determine the peak velocity and radius. Whether a satellite induces bar formation also depends on other factors, such as the kinematic temperature of the inner disk and the orbit of the satellite (see, e.g., M. K. Cavanagh & K. Bekki 2020). Thus, the choice of Γ in this section is not meant as an ultimate lower limit, but is instead used to select satellites of interest in each of the FIRE-2 simulations. If we set a lower limit on the tidal index Γ, we will find more satellites, but none of those seem to lead to bar formation within 10 dynamical times. We explore the effects of varying this limit in Γ in Appendix F.

We consider a satellite with sufficiently high Γ to be the trigger of bar formation if the bar begins forming within 10 dynamical times of its pericentric passage. We also calculate the angle between the satellite orbital angular momentum and the spin of the disk, $\cos\theta_{\rm orbit} = \hat{j}_{\rm orbit} \cdot \hat{j}_\star$, where $\cos\theta_{\rm orbit} = +1$ for a perfectly prograde orbit, -1 for a perfect retrograde orbit, and 0 for a perfect polar orbit. Prograde satellite encounters are considered more likely to trigger bar formation (E. L. Łokas 2018), but we include all satellite orbits in our analysis for now. In Appendix F, we describe the detailed steps we follow to determine which satellites meet the criteria outlined above using the scaled tidal index, and in Table 4 we summarize the properties of the satellites in FIRE-2 galaxies.

In Figure 6, we show the three FIRE-2 simulations (m12f, m12b, and m12r) that had satellite encounters meeting these criteria. In the top panels, we show the evolution of bar strength as a function of disk radius ($R < 10$ kpc) in time. The color bar represents the bar strength, A_2/A_0, for each simulation. In the bottom panels, we show the evolution of the scaled tidal index Γ for each satellite that meets the criteria. The different colored lines indicate the different satellites within each simulation. Consistent with prior work, all satellites that meet our criteria are on prograde or partially prograde orbits ($0 < \cos\theta_{\rm orbit} < 1$).

All simulations in Figure 6 have bars in the central regions of the disks, which appear as dark red patches within $r < 2$ kpc in the top panels. Similar dark red patches in the outer parts of the disks are either spiral arms or other deformations of the stellar density from an azimuthally symmetric distribution during the satellite interaction.

Below, we discuss each of the cases in Figure 6 in more detail.

m12f. In Figure 6, one of the massive satellites in m12f (the blue line in the bottom panel) undergoes close pericentric passage with the disk and interacts for more than a gigayear before attaining a maximum tidal index of $\Gamma = -0.53$ at the time of merger at 12.4 Gyr (the time when A_2/A_0 crosses 0.1). This event forms the strongest bar among all the FIRE-2 galaxies. During the merger, the mass ratio of the stellar disk of the host to the satellite is $M_{\star,\rm host}/M_{\rm sat} = 0.5$ and this event causes a large perturbation in the outer disk (note the dark red patches in the outer disk that coincide with the black vertical line tracing the merger). These perturbations propagate to the inner disk. The bar grows stronger (the dark patch within radius $r < 2$ kpc, around 13 Gyr) after the merger. After 13.6 Gyr, the bar weakens significantly and the bar strength dips below 0.1 in the last 0.11 Gyr of evolution (see Figure 4).

m12b. The bar in m12b is lopsided (Figure 2) and grows inside out, maintaining its lopsidedness over a period of more than 5.7 Gyr (Figure 6), even as it increases in size. See E. L. Łokas (2021), where the authors study lopsided bars in cosmological simulations. One of the massive satellites in m12b, which has $M_{\rm sat} = 6.1 \times 10^{10}\ M_\odot$ at pericenter with $\Gamma = -2.3$ (the blue curve in Figure 6), interacts with the disk for more than 2 Gyr, during which it undergoes two pericentric passages, before merging with the disk at 10.9 Gyr. The rise and fall of the bar strength is in phase with the two pericentric passages. By the time the satellite ultimately merges with the disk, its mass has decreased to one-eighth the disk mass at $D_{\rm H} = 14.8$ kpc, yielding $\Gamma = -3.39$ (see Table 4), and is no longer massive enough to affect the bar.

The bar gains strength again via internal evolution and remains in the disk until the end of the simulation. Other than the above satellite, m12b undergoes multiple satellite interactions of lower Γ between 7 and 12.5 Gyr (not shown in Figure 6). As a result, large perturbations appear in the outer disk throughout its evolution.

m12r. Not all strong satellite interactions lead to the formation of a strong bar. Galaxy m12r undergoes multiple satellite interactions, two of which are on highly prograde orbits ($\cos\theta_{\rm orbit} \sim 0.9$) and have high tidal indices that disturb and distort the outer disk (the thick blue line with $\Gamma_{\rm max} = 0.61$ and the golden line with $\Gamma_{\rm max} = -0.22$ in Figure 6; see also Table 4). The pericentric passage of the satellite close to

Table 4
Satellites in FIRE-2 Galaxies

Name	$\frac{A_2}{A_0}_{\max}$	$\log_{10}\left(\frac{M_{\rm sat}}{M_\odot}\right)$	$D_{\rm H}$ (kpc)	$\frac{M_{*,\rm host}(r<D_{\rm H})}{M_{\rm sat}}$	Tidal Index Γ	$\cos\theta_{\rm orbit}$	Time of Merger (M) or Pericenter (P) (Gyr)	Time of $\frac{A_2}{A_0}=0.1$ (Gyr)
(1)	(2)	(3)	(4)	(5)	(6)	(7)	(8)	(9)
Simulations with bars affected by satellites								
m12f	0.203	10.97	4.44	0.50	−0.53	0.99	12.38 (M)	12.38
m12b	0.182	11.21	39.1	0.36	−3.42	0.07	8.78 (P)	8.06
		10.79	12.01	1.08	−2.3	0.92	10.44 (P)	…
		9.96	14.81	7.6	−3.39	0.84	10.96 (M)	…
		9.29	12.16	40.5	−3.81	−0.94	12.43 (P)	…
m12r	0.133	9.63	5.17	2.29	−0.22	0.94	13.37 (M)	12.92
		10.69	7.13	0.18	0.42	0.99	12.64 (P)	…
		10.47	5.21	0.29	0.61	0.88	13.01 (P)	…
		10.78	7.54	0.19	0.43	0.94	13.11 (M)	…
Simulations with bars not significantly affected by satellites								
Romeo	0.144	8.42	8.7	187	−3.52	−0.60	10.24 (P)	12.64
		9.1	17.08	50.11	−3.71	−0.04	10.92 (P)	…
Remus	0.113	10.23	26.34	6.36	−3.99	0.19	13.64 (P)	12.22
		9.56	20.55	22.4	−4.34	0.22	10.65 (P)	…
m12m	0.112	8.9	18.54	129	−3.45	−0.42	11.64 (P)	12.96
		9.2	56.26	76.6	−4.61	0.33	12.77 (P)	
m12w	0.163	7.14	6.66	3206	−4.47	0.39	12.73 (P)	13.66
m12c	0.123	11.02	18.12	0.58	−1.87	0.79	12.89 (P)	13.73
		7.81	5.85	699	−3.61	−0.22	13.78 (M)	…
Simulations with weak bar-like perturbations								
m12i	0.092	9.58	29.99	9.1	−4.46	−0.73	9.86 (P)	…
		9.08	10.43	25.48	−3.57	−0.53	7.79 (P)	…
Thelma	0.082	10.53	7.26	0.49	0.79	0.89	8.01	…
		9.80	3.38	1.58	1.06	0.06	8.11	
Simulations without bars								
Romulus	0.07	10.18	41.41	4.27	−5.26		7.74	…
		9.14	8.87	25.65	−4.29		6.61	
Louise	0.06	10.29	5.12	0.93	2.33		13.48	…
Juliet	0.05	10.23	35.45	2.46	−4.43		13.10	…
		8.22	6.99	139.3	−4.32		8.32	

Note. Summary of the massive ($M_{\rm halo} > 10^7 M_\odot$) satellite interactions with varied tidal index Γ in the FIRE-2 galaxies that induce bar formation in some galaxies during merger or pericenter passage and in some galaxies do not. The table has four parts, with the galaxies in each separated by horizontal lines: (1) galaxies that undergo interactions with satellites with $\Gamma > -2.45$ at pericenter and form bars (m12f, m12b, and m12r); (2) galaxies that form bars but not due to satellite interactions (Romeo, Remus, m12m, m12w, and m12c); (3) galaxies that undergo strong interactions (not during the growth of A_2/A_0) but only form weak bar-like perturbations (m12i and Thelma); and (4) galaxies that do not form bars but have strong bulges that hinder bar formation, even with strong satellite interactions. Column (1): name of the simulation. Column (2): peak bar strength. Column (3): M_{200} mass of satellite in log scale. Column (4): distance of the satellite from the host galaxy center (at pericenter or merger). Column (5): mass ratio of the satellite and the host galaxy within a radius of $D_{\rm H}$ from the host center. Column (6): the tidal index Γ at pericenter or merger (Equation (7); see Section 4.1). Column (7): cosine of the angle between the angular momentum vector of the satellite orbit and the disk angular momentum. Column (8): time of the merger (M) or pericenter passage (P) of the satellite. Column (9): time when the bar strength crosses $A_2/A_0 = 0.1$, i.e., when the bar forms. If the time interval between the time of the interaction (merger or pericenter passage) and the time of bar formation is greater than 10 dynamical times, we do not associate bar formation with satellite interaction.

12.6 Gyr (in blue) raises A_2/A_0 in the outer disk ($r > 3$ kpc) and increases the bar strength in the inner disk ($r < 2$ kpc). This satellite's final pericentric passage at 13.11 Gyr has $\Gamma = 0.43$, one of the highest values of any interaction in the simulation suite. Another satellite in a highly prograde orbit ($\cos\theta_{\rm orbit} = 0.9$) with high tidal index ($\Gamma = -0.22$; shown in gold) merges with the disk at nearly the same time (13.37 Gyr). These strong tidal interactions with multiple satellites create large asymmetries in stellar density that are also observed in A_2/A_0. A weak, short bar is seen to form momentarily in the inner disk of m12r, but is quickly dissipated under the strong tidal forces, consistent with results from N-body simulations showing that mass ratios above $M_{\rm sat}/M_{\rm host} \sim 0.1$ are not conducive to bar formation (e.g., M. K. Cavanagh & K. Bekki 2020). In Section 4.2.2, we explore further the transient nature of the bar in m12r.

4.2. Bar Formation from Disk Internal Evolution

Five of the FIRE-2 galaxies host bars that do not form through any kind of satellite interaction (merger/pericenter) but during the internal evolution of the disk (Table 4). In addition, only some of the bars in other galaxies are instantiated by a

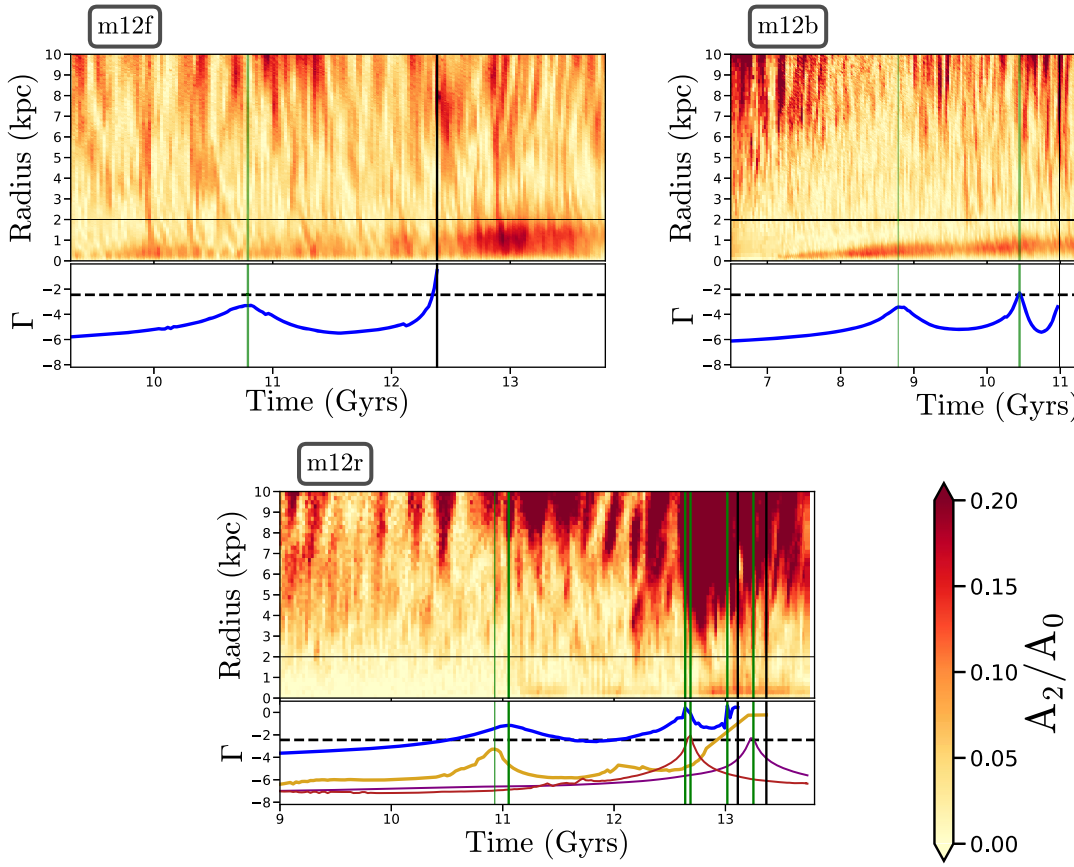

Figure 6. Bar formation due to satellite interaction in m12f, m12b, and m12r. The upper halves of all panels show the evolution of the bar strength (A_2/A_0) with time (in gigayears), at different radii (in kiloparsecs) of the stellar disk. The color bar shows the range of bar strength, $0.0 < A_2/A_0 < 0.2$, where yellow is for the lower limit and dark red is for the upper limit. The dark red patch in the central region (radius <2 kpc) shows the presence of the bar. The dark red stripes at the outer part of the disk may be perturbations, due to the interaction of different satellites (black lines for mergers and green lines for pericenter passage) or due to transient spiral arms in the disk. The lower halves of each panel show the evolution of the tidal indices Γ (*y*-axis; Equation (7)) of the satellites with $\Gamma > -2.45$ (dashed horizontal line; see Section 4.1) at least once during evolution. The *x*-axis is time (in gigayears). The blue thick curve of Γ evolution shows the strongest satellite interaction in each system. In m12r, a satellite with a similar maximum tidal index as the blue one is shown in the golden color. The thick vertical lines (black and green) represent the strongest tidal impact interactions, while the thin lines are for smaller tidal index satellites. The dashed vertical lines represent the retrograde motion of the satellite with respect to the stellar disk (see the details in Table 4). For more details on each system, see Section 4.1.

satellite passage. In Figure 7, we present the evolution of the bar strength A_2/A_0 with radius and time for the galaxies m12m, Remus, m12w, m12c, and Romeo. The bar length and strength (reddish color) in the central regions of the disks ($r < 2$ kpc) appear to oscillate at several frequencies, and the outer regions of the disks in Remus and Romeo are much less perturbed compared to the disks hosting bars that form through satellite interactions in Figure 6. This is unsurprising, since these galaxies have far fewer satellite interactions than those hosting bars triggered by satellites, and of those even fewer have high tidal index Γ (Table 4). None of the satellites in these systems meet the two criteria for bar formation outlined in Section 4.1 simultaneously. For example, one of the satellites in m12c has a pericenter passage with tidal index $\Gamma = -1.87$, which fits the first selection criterion, but a bar does not form for more than 20 dynamical times after this interaction, so we consider it uncorrelated with bar formation.

In the absence of satellite interactions, the bar strength grows from the center outward, showing oscillations in A_2/A_0 at multiple frequencies. Once formed, the bar persists until the end of the simulation for Remus, m12w, and m12c but dissolves for Romeo and m12m. The bar in m12w appears to form in somewhat unique circumstances, as gas is expelled from the central region during an epoch of a high star formation rate. As the gas content decreases, a rectangular bar arises in the disk at 13.6 Gyr and stays until the end of the simulation.

All five bars in Figure 7 have lower $A_2/A_{0,\max}$ than the bars in Figure 6 formed through satellite interactions. It is complicated to directly predict the $\mathcal{R}$ ratio of a bar that is satellite-induced, compared to a bar that forms during internal evolution (T. Miwa & M. Noguchi 1998; E. L. Łokas et al. 2016; I. Martinez-Valpuesta et al. 2017), but here we find that bars formed through satellite interaction have lower $\mathcal{R}$ ratios ($R_{\rm co}/a_s$) than bars formed through internal evolution (see Table 3).

Given that FIRE-2 galaxies can clearly form bars through internal processes, we now consider which properties of the central region create favorable conditions for bar formation to occur via internal evolution. Are the intrinsic properties of the galactic disk and DM halo playing any role that makes it more likely for bars to form in some disks rather than others or in the eventual length and strength of the bar? To address these questions, we look at a variety of disk properties for the simulations that form bars through internal processes: the central density and concentration of stars, gas, and DM (Section 4.2.1); the kinematic coldness of the disk (Section 4.2.2); and the role of gas fraction and stellar feedback (Section 4.2.3).

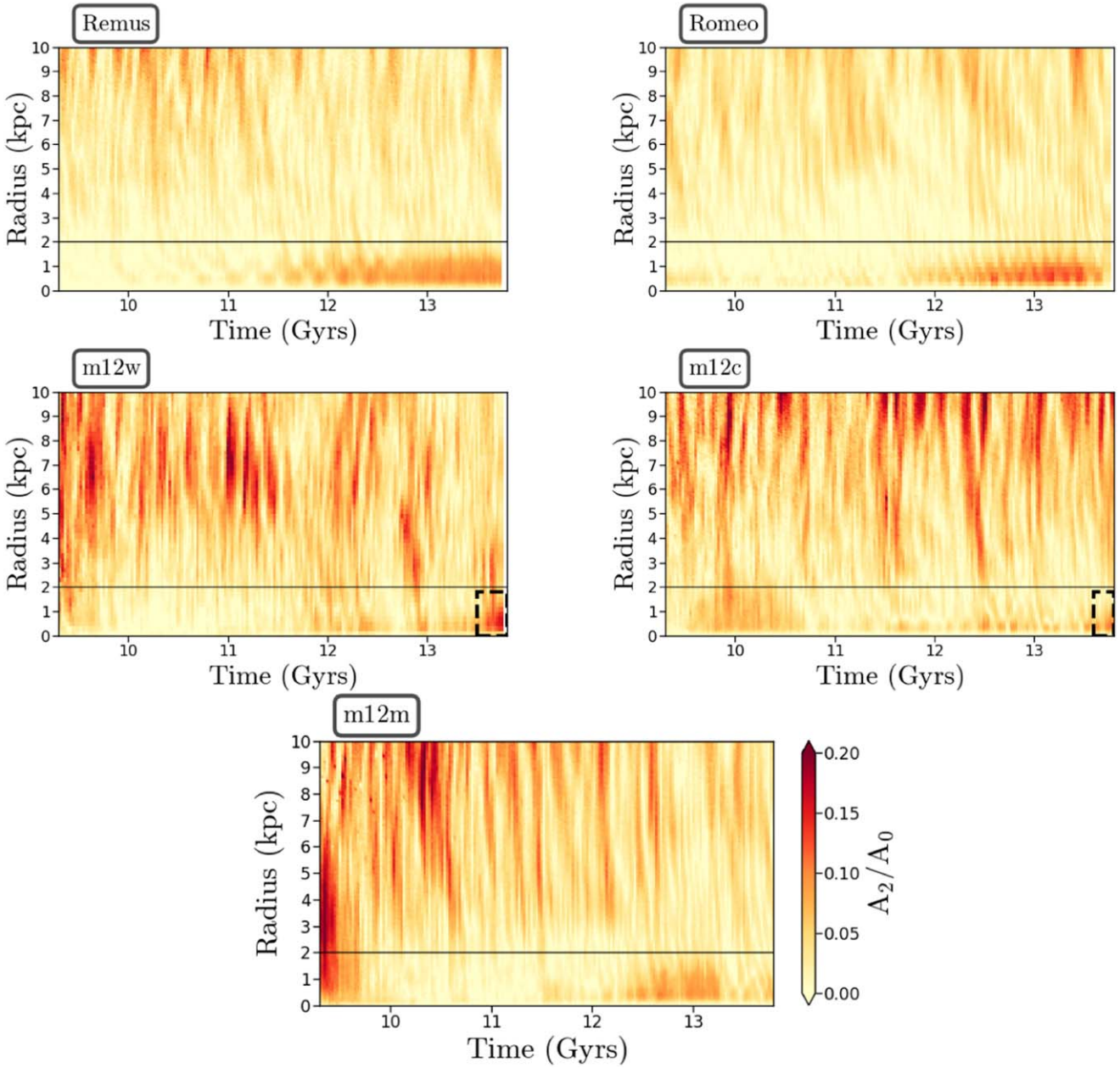

Figure 7. Bar formation during the internal evolution of the disk in Remus, Romeo, m12w, m12c, and m12m. Similar to Figure 6, the dark patch in the central region (radius <2 kpc) shows the presence of the bar. We highlight the bars in m12w and m12c with dashed rectangles, as their time duration is short. The dark red stripes at the outer part of the disk are perturbations. In these five cases, either the satellite interactions are less impactful (seen from the very calm outer disk for Remus and Romeo) or the time between the satellite interaction and rise of the bar strength above 0.1 is more than 10 dynamical times (m12w, m12c, and m12m). However, bar instabilities arise in the disk. In Appendix G, we present the satellite interactions that have failed to trigger bar instability in Remus, Romeo, m12w, m12c, and m12m.

4.2.1. The Central Density Profile

We examine the central mass profiles of stars, gas, and DM in the FIRE-2 disks to investigate their effect on bar formation, since the relative distribution of stars, gas, and DM in the central galaxy has a significant effect on bar properties (E. Athanassoula 2002). E. Athanassoula & A. Misiriotis (2002) show that stronger, more rectangular bars form in more DM-dominated disks, provided there is interaction between the DM halo and the disk (E. Athanassoula 2002). Furthermore, a standard condition for swing amplification of a bar instability is a rising central rotation curve that is dominated by the stellar circular velocity at the peak and falls to the circular velocity of the DM halo at higher radii (G. Efstathiou et al. 1982; V. P. Debattista & J. A. Sellwood 1998; O. F. Marioni et al. 2022).

In Section 2, we presented the total circular velocity profiles of all the FIRE-2 galaxies (see Figure 1). In Figure 8, we present the rotation curves and mass profiles in the inner 10 kpc of the FIRE-2 galaxies separated by species (stars, gas, and DM). The top panel of Figure 8, which shows the rotation curves, shows that the barred and unbarred galaxies in FIRE-2 have sharply rising stellar circular velocity curves (panel (a)) that dominate over the DM (panel (b)) and gas (panel (c)) components, in agreement with bar instability theory. For example, in m12f, the circular velocity of the DM component

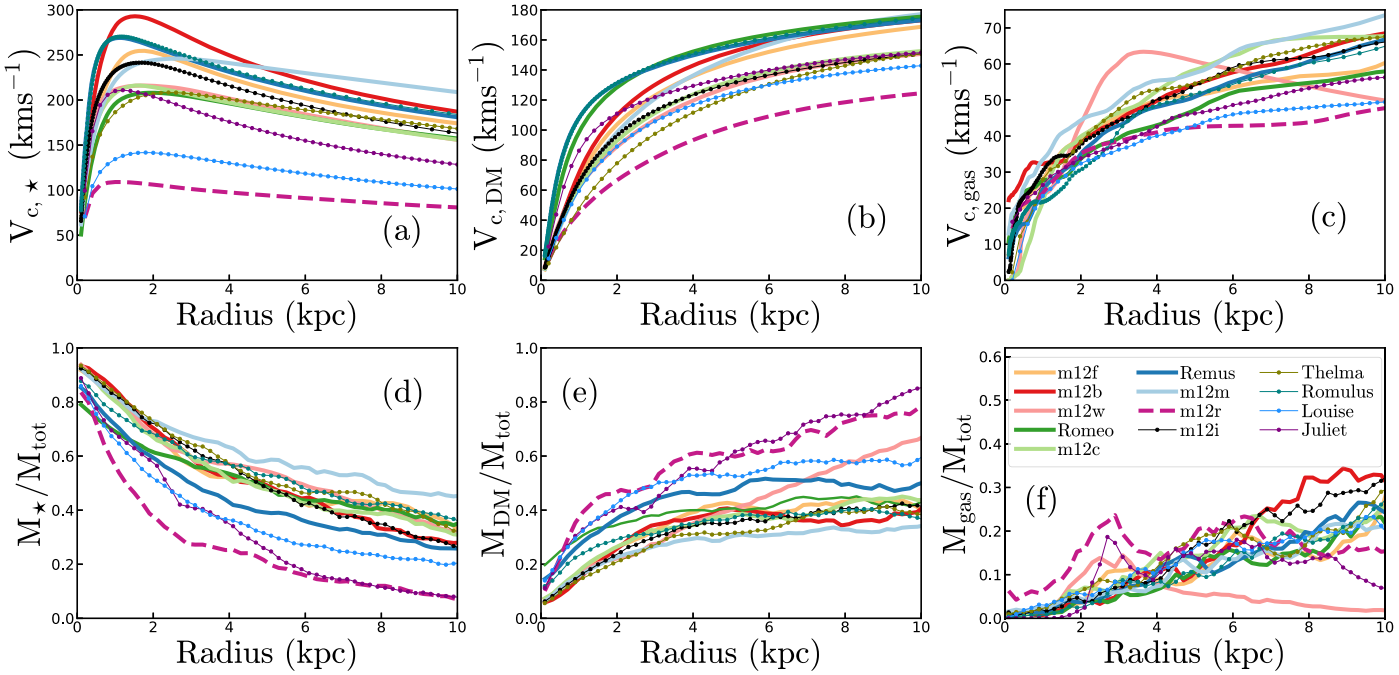

Figure 8. Rotation curves and mass fractions. The top row (panels (a)–(c)) shows rotation curves (Equation (1)) of all the FIRE-2 galaxies at their peak bar strengths for stars (a), gas (b), and DM (c); the bottom row (panels (d)–(f)) shows relative mass fractions of different species within $|z| \leqslant 2$ kpc for the same species. All quantities are plotted as a function of spherical radius r (not cylindrical R). The thick lines represent the barred galaxies, and the thin lines with circular markers represent unbarred galaxies. The thick dashed line is for m12r, which is significantly less massive than all other galaxies. Note that the vertical axis range is different for each component.

rises slowly and matches the circular velocity of the stellar component at a radius of ∼10 kpc. m12f has $R_{90} = 11.8$ kpc (Table 1) and within nearly this entire region the mass distribution is dominated by the stellar component. The other FIRE-2 galaxies are similarly baryon-dominated at the center.

In the bottom row of Figure 8, we show the mass fractions of the different components with radius. Similar to the results from the circular velocity curves (top row), we find that FIRE-2 galaxies have more stars than DM in their centers (panels (d) and (e)). However, we do not see any prominent difference in mass fractions between the barred and unbarred galaxies in FIRE-2. Hence, the barred and unbarred galaxies have similar proportions of their mass in stars, DM, and gas. Interestingly, the central gas mass fraction contributes significantly to the rotation curve (panels (c) and (f)), which is thought to suppress bar formation (K. L. Masters et al. 2012; see Section 4.2.3).

We also compare the bar length to the radius corresponding to the peak of the circular velocity curves ($R_{\rm max}$). The peak circular velocity for the barred galaxies is in the range $V_{\rm max} \sim 147-316\,{\rm km\,s^{-1}}$ and the corresponding radius $R_{\rm max} \sim 1.5-9.8$ kpc, with m12r, the lowest-stellar-mass galaxy, having the lowest peak velocity $V_{\rm max} = 147\,{\rm km\,s^{-1}}$ and largest radius $R_{\rm max} = 9.8$ kpc in our sample. Nearly all the bars have $R_{\rm max} > a_s$; in other words, they lie within the rising part of the total circular velocity curve (except Remus; see Table 1 and Table 3). Furthermore, the peak circular velocity ($V_{\rm max}$) is greater than the maximum circular velocity of the DM halo in all systems except for m12r, another classic criterion for bar formation (G. Efstathiou et al. 1982; V. P. Debattista & J. A. Sellwood 1998), although not a sufficient criterion (G. Efstathiou et al. 1982; O. F. Marioni et al. 2022).

Additionally, we investigate the density profile of the DM component of the barred and unbarred galaxies in FIRE-2 to examine the role of the DM density in the central region close to the disk (also see A. Lazar et al. 2020). Figure 9 shows the DM density profile $\rho_{\rm DM}(r)$ (in $M_\odot{\rm kpc}^{-3}$, in log scale) as a function of radius (in kiloparsecs) of the FIRE-2 galaxies, using the same color scheme and line style as Figure 1. Figure 9 shows that the barred and unbarred galaxies both have flat or "cored" central density profiles with a range of maximum densities. There is no distinct difference between the barred and unbarred galaxies, which means that the DM density profile is not an indicator of barred/unbarred disk morphology in this sample. However, preliminary studies using N-body simulations show that cored DM profiles are less likely to form strong bars compared to cuspy DM profiles (S. Ansar et al., in preparation).

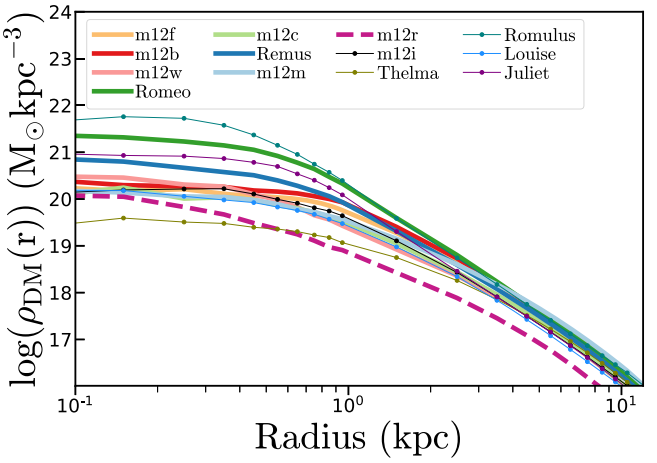

Figure 9. Cores in the DM density profile at peak bar strength. The thick lines represent barred galaxies, the thin lines show unbarred galaxies, and the thick dashed line shows m12r (one of the lowest DM densities). The central density profiles are similar for barred and unbarred systems.

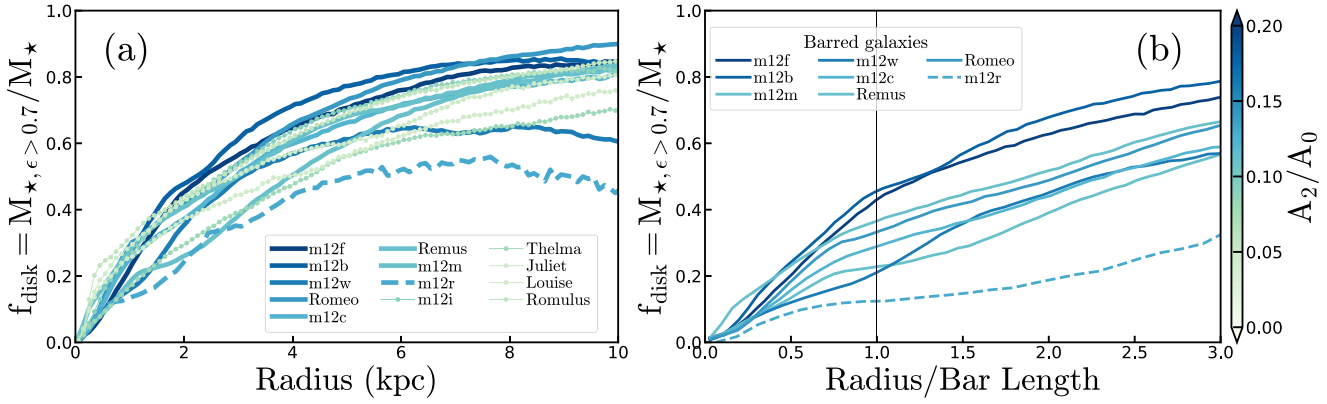

Figure 10. Kinematically colder disks host strongly barred galaxies. Higher $f_{\rm disk}$ shows the large fraction of star particles in rotational orbits in the disk plane, which is a proxy for a kinematically cold disk that is prone to bar instability. Panel (a): $f_{\rm disk}(r)$ profile of all FIRE-2 galaxies at their peak bar strengths, with the annular bin size of $\Delta R = 0.1$ kpc. Panel (b): the same $f_{\rm disk}(r)$ profile for the barred galaxies at their peak bar strengths, with the x-axis scaled by the bar length. The black vertical line denotes the edge of the bar for all the galaxies. In panel (a), the thick lines are for barred galaxies and thin lines with solid circles are for unbarred galaxies. In both panels, the galaxies are color coded with the value of their peak bar strength from the color bar of A_2/A_0. Strongly barred galaxies (for example, m12f and m12b) are kinematically colder compared to weakly barred ones (for example, m12m and Romeo). The dashed line in both panels is for m12r, which has very different properties than the rest of the galaxies.

The slow-rising DM component of the rotation curve in most of the FIRE-2 galaxies can explain why bars formed in FIRE-2 galaxies are more rounded and less rectangular, similar to the idealized N-body model MD in E. Athanassoula & A. Misiriotis (2002), which forms a rounded bar in a stellar disk with similar mass and a slow-rising DM component. The more rounded bar morphology also results in lower bar strength A_2/A_0, which shows a higher amplitude for rectangular bars. However, *all* the FIRE systems, both barred and unbarred, fit many of the classic criteria for bar formation, with few obvious differences between the two groups, and all have similarly cored DM profiles that have previously been associated with weaker bars. Thus, the relative distribution and concentration of the stars, gas, and DM can explain the shape, and perhaps the weakness, but not the origin of the bars in FIRE.

Round-shaped bars have been found in the 3.6 μm Spitzer images of barred galaxies (P. Erwin et al. 2023). Even though we do not conduct synthetic observations, the old stellar population observed in 3.6 μm images can be compared to the bars in the simulations. The bar major-axis stellar surface density profiles of the FIRE-2 galaxies are similar to the "two-slope" and "flat-top" types of bar profile in P. Erwin et al. (2023; see Figure 23 in Appendix H).

4.2.2. The Kinematic Coldness of the Disk

In idealized disk galaxy simulations, "kinematically cold" disks with a high fraction of stars in rotational motion in a common plane are the most susceptible to the bar instability (J. P. Ostriker & P. J. E. Peebles 1973). To determine whether this is so in our simulations, we measure the fraction of stellar mass that contributes to rotationally supported orbits in near circular motion in the disk plane, $f_{\rm disk}$, as a proxy for kinematic coldness. To estimate $f_{\rm disk}$, we calculate the circularity $\epsilon = j_{z,i}/j_{{\rm circ},i}(E_i)$ (defined in M. G. Abadi et al. 2003) for each star particle i in the disk with cylindrical radius $R < 10$ kpc and $|z| \leqslant 2$ kpc. Here, $j_{z,i} = j_{{\rm z},i} \cdot j_{\rm net}/|j_{\rm net}|$ is the component of the specific angular momentum of the ith star particle toward the direction of the total specific angular momentum $j_{\rm net}$ of the disk (also see K. El-Badry et al. 2018), and $j_{{\rm circ},i}(E_i)$ is the specific angular momentum of the circular orbit with the same energy E_i as the star particle. The maximum specific angular momentum an orbit can have is for a circular orbit, so ϵ lies between ± 1, with $+1$ indicating a prograde circular orbit and -1 a retrograde circular orbit in the galaxy disk's plane. A value of $\epsilon \sim 0$ can represent either a circular orbit nearly perpendicular to the disk plane or a radial orbit.

The energy E_i can be written in terms of the radius $R_{c,i}$ of the circular orbit in the plane of the disk with the same energy as the star particle i:

$$E_i = \frac{GM(r < R_{c,i})}{2R_{c,i}} + \Phi(R_{c,i},\, 0); \tag{8}$$

the corresponding specific angular momentum is

$$j_{\rm circ}(E_i) = R_{c,i} V_{c,i}(R_{c,i}) = \sqrt{GM(r < R_{c,i}) R_{c,i}}\,. \tag{9}$$

Here, $\Phi(R_{c,i},\, 0)$ is the total potential due to all components evaluated at radius $R_{c,i}$ in the disk plane. For each star particle, we calculate E_i, $R_{c,i}$, and $j_{{\rm circ},i}(E_i)$ to obtain ϵ_i for each star and calculate the mass fraction of stars with circularity greater than 0.7; that is, $f_{\rm disk}(r) = M_{\star,\epsilon>0.7}/M_\star$, in annular radial bins of width $\Delta R = 0.1$ kpc.

Figure 10 shows $f_{\rm disk}$ as a function of disk radius R, for all the galaxies in our FIRE-2 sample at $z_r = 0$ (panel (a)) and separately for the barred galaxies only (panel (b)) at their peak bar strength, which is at a different time for each galaxy. The line color in panel (b) is proportional to the maximum bar strength. Overall, kinematically colder disks with high $f_{\rm disk}$ and galaxies with strong satellite interactions (for example, m12f and m12b) form stronger bars than the cold disks without any strong satellite interactions (for example, m12m, Remus, and Romeo) in the FIRE-2 galaxy sample. The central regions of the disks are also clearly kinematically hotter than the outer disks in all the galaxies.

To establish a causal connection between the kinematic coldness of the stellar disk and bar strength, we consider the evolution in time of the bar strength and kinematic coldness at different radii for all 13 FIRE-2 galaxies. We expect the bar strength A_2/A_0 to be anticorrelated with the coldness parameter $f_{\rm disk}$, with the bar growing in strength after the disk becomes cold. We find that the disks in the FIRE-2 galaxies have a broad range of kinematic temperatures. In Figure 11, we present some

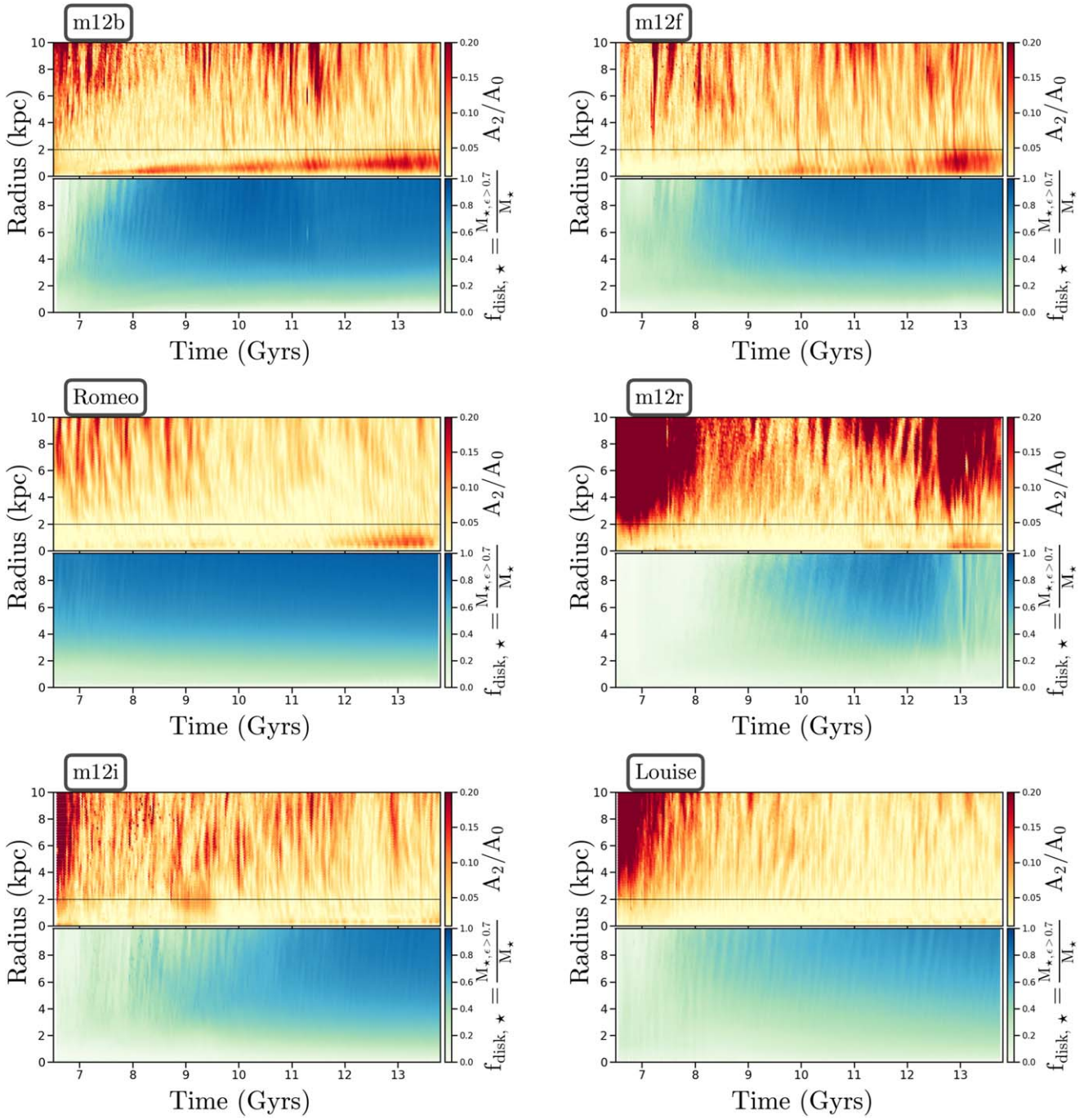

Figure 11. Stronger bars in kinematically colder disks. The history of the bar strength (A_2/A_0) evolution (top panels for each simulation with color bar for bar strength: $0.0 < A_2/A_0 < 0.2$) along with the kinematic coldness parameter $f_{\rm disk}(r) = M_{\star,\epsilon\ >\ 0.7}/M_\star$ of the stellar disk (bottom panels for each simulation with color bar: $0.0 < f_{\rm disk} < 1.0$) for all the barred galaxies in FIRE-2. In the lower halves of all panels, the higher the $f_{\rm disk}$ value, the colder is the disk. Lighter shades of gray show high $f_{\rm disk}$, darker shades of blue show very low $f_{\rm disk}$, while the different shades of orange, green, and purple have intermediate values of $f_{\rm disk}$. This figure shows examples of bars forming during satellite interactions (m12b and m12f) and internal evolution (Romeo) in kinematically cold disks; a weak, short, and transient bar in a kinematically hot disk (m12r); a failed bar (m12i); and an unbarred galaxy with a bulge and kinematically hot disk (Louise).

instructive examples across this range; similar plots for all 13 galaxies are shown in Figures 24 and 25 of Appendix I. The color scheme for the bar strength is the same as in Figures 6 and 7. For $f_{\rm disk}$, we use darker shades of blue for kinematically cold regions of the disk, while lighter shades of blue and green show the kinematically hot regions (see Figure 11).

m12b and m12f (the top row of Figure 11) are the strongest barred galaxies in the sample, and both have very kinematically cold stellar disks. The bar in m12b begins to form around 7.5 Gyr, just as the disk has become significantly cooler. When m12f reaches a similar coldness, around 9.5 Gyr, a bar also begins to grow, although it does not get very strong until a satellite interaction around 12.7 Gyr. Both m12f and Romeo (middle row, left panel) show that even if the disk is very kinematically cold, the bar subsequently formed by internal evolution is not very strong (other examples are m12m and Remus, both shown in Figure 24). m12r (middle row, right panel) forms a weak, short bar in a kinematically hot disk only

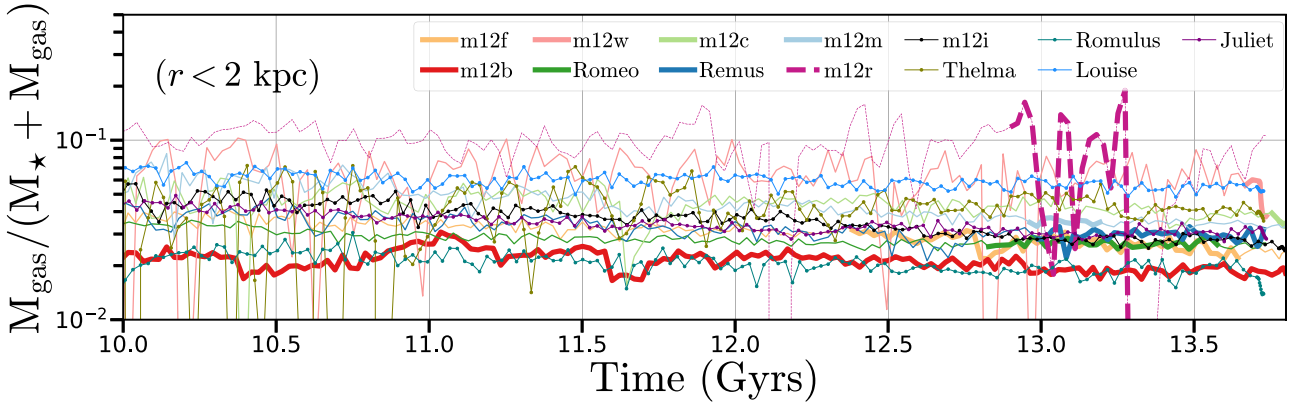

Figure 12. Evolution of central gas fraction for barred and unbarred galaxies. Each line shows $M_{gas}/(M_{gas} + M_\star)$ in the central region of the disk ($R < 2$ kpc and $|z| < 1$ kpc). As in Figure 1, the thin lines with solid circles are for unbarred galaxies and the dashed magenta line is for m12r. The thick lines are for the "bar episodes" in the barred galaxies. No trend in barred vs. unbarred systems is at first apparent, but m12w (pink) and m12r (dashed magenta), the two weak bars, have high gas fractions that vary substantially with time, while the two strongest bars, m12f (orange) and m12b (red), have low gas fractions that are relatively steady in time.

after a strong satellite interaction, around 12.7 Gyr. This bar quickly fades out as it is dissolved by the high fraction of random motion. In the absence of a strong external perturbation, the kinematically hot disks in our sample—such as m12r, m12i, and Louise (bottom row, left panel)—do not form bars (see also Juliet and Romulus in Figure 25). Thus, we find that in the cosmological environment of galaxy evolution, the kinematic coldness of the disk is still an important factor in bar formation. Although a cold disk by itself does not appear to be a sufficient condition for bar formation, it is clearly a necessary one for bars that form via internal evolution. The lifetime of a bar after it forms, whether due to internal evolution or satellite interaction, also depends on the state of the kinematic coldness of the disk.

Additionally, we note that F. McCluskey et al. (2024) showed that $v_{\phi,\star}$, $\sigma_\star$, and $v_{\phi,\star}/\sigma_\star$ for "young stars" in FIRE-2 agree well with M31, M33, for galaxies in the PHANGS survey, and in the cold gas. There are no evident signs that the gas or young stars in the FIRE-2 galaxies are too hot dynamically. However, this may have some tension with the MW and the old stars that the authors did not compare with.

4.2.3. Gas Fraction and Stellar Feedback

Observational studies have shown that bars are less likely to form in gas-rich star-forming galaxies and are instead mainly found in gas-depleted red galaxies (F. D. Barazza et al. 2008; K. L. Masters et al. 2012). The gas fraction in the disk is expected to affect the morphological properties of bars, and bar formation in a gas-rich disk is thought to proceed more slowly (E. Athanassoula et al. 2013). As shown in Figure 12, the FIRE-2 galaxies mostly have a mass fraction of nearly 10% in gas in the central 2 kpc and would likely not be considered gas-depleted. There is also a significant amount of gas infall and outflow in the central regions of the FIRE-2 galaxies, driven by feedback from star formation. Consequently, the central gas fraction $M_{gas}/(M_{gas} + M_\star)$ fluctuates rapidly, modifying the disk potential on freefall timescales.

In Figure 12, we show the evolution of the gas fraction $M_{gas}/(M_{gas} + M_\star)$ in the central region ($r < 2$ kpc) of the disk for each of the FIRE-2 galaxies. The color scheme and line thickness are same as in Figure 1. We use thin lines with solid circles for unbarred galaxies, thick lines for "bar episodes," thin lines for the unbarred phases in the barred galaxies, and a thick dashed line for m12r.

In Figure 12, we find that m12w (in pink) and m12r (dashed magenta line) have the highest gas fractions, which also vary the most compared to the other galaxies. Our investigation shows that m12w and m12r undergo repeated episodes with large fluctuations in the star formation rate over a short time interval.

This rapid change in the star formation rate (within $R < 2$ kpc) leads to rapid fluctuations in the feedback strength and hence in the gas fraction (K. El-Badry et al. 2016; M. E. Orr et al. 2018; S. Yu et al. 2021; A. B. Gurvich et al. 2023). These changes in gas fraction alter the ability of the galaxy to form a bar. For example, in m12w, a bar forms immediately following a large outflow of gas (Figure 13), which itself is induced by a strong interaction with a satellite. Similarly, m12r undergoes a strong tidal interaction with a satellite galaxy that forms a bar, but has a high gas fraction that should suppress bar formation, and indeed the bar dissolves rapidly. Conversely, the barred galaxies with the highest strengths, m12f (in orange) and m12b (in red), show the lowest gas fractions by the end of their evolution.

Rapid, quasiperiodic fluctuations in the gas fraction near the galaxy center, driven by feedback processes, can destabilize bar orbits by modifying the central potential, as a result of the mass redistribution of gas. For more discussion on fluctuations in potential affecting bar formation, see Section 5.3.

5. So Why Are FIRE Bars Weak and Short?

A superficial comparison with the bars arising in the zoomed cosmological simulations of MW-mass galaxies from Auriga (F. Fragkoudi et al. 2021) reveals that the bars that arise in the FIRE-2 galaxies appear much weaker ($A_2/A_0 \lesssim 0.2$) and more ellipsoidal. We caution that although the two suites share similar particle mass resolution, many other choices in the numerical models are quite different, especially the representation of the multiphase ISM and clustered nature of star formation (we do; they do not), the locality of stellar feedback (scales of 3 versus 100 pc), and whether AGN feedback is included (we do not; they do). Taken together, these differing choices lead to both small- and large-scale differences in the environment of the inner galaxy that can explain the differences in the types of bars that are formed. Broadly, the stellar

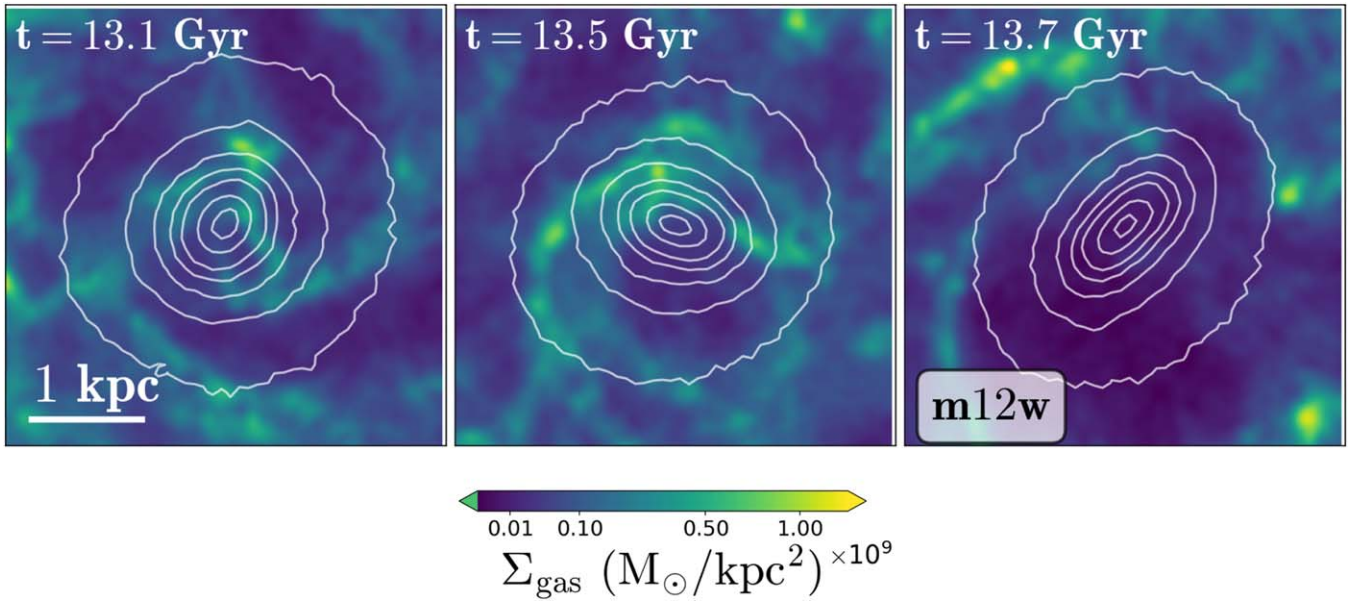

Figure 13. Bar formation following the removal of gas in the inner galaxy. In all three panels, the white contours show the face-on stellar distribution in the inner 4×4 kpc^2 region of m12w and the color map corresponds to the gas surface density (blue = low, yellow = high). Left: large gas fraction in the center and no bar structure in the stellar component. Center: as gas begins to flow out of the center, a bar structure begins to emerge. Right: gas evacuated from the center and a strengthening bar in the stellar component.

feedback model in Auriga leads to a smoother ISM, smoother star formation, and less core formation, which may lead to the formation of stronger bars.

5.1. Do the Bars Buckle During Evolution?

Buckling is a dynamic process in barred galaxies where a bar initially forms an asymmetric structure that extends out of the disk plane, eventually evolving into a thickened boxy/peanut bulge, clearly visible from an edge-on view (V. P. Debattista et al. 2006; A. C. Quillen et al. 2014; J. A. Sellwood & O. Gerhard 2020). When applying standard probes of bar buckling (V. P. Debattista et al. 2006; K. M. Xiang et al. 2021) on the FIRE-2 bars, we observe some of the measures showing signatures of buckling in some cases, while some other probes do not detect any buckling event in those cases. Even though one of the m12m simulation runs studied in V. P. Debattista et al. (2019) shows the presence of the X-shaped bar, a buckling event has not been confirmed as the origin of the X shape. All X/peanut shapes may not originate from a buckling event (X. Li et al. 2023). Furthermore, buckling events have been studied thoroughly for strong bars but not for weak bars, as in the case of FIRE-2. The evidence for bucking in these bars is ambiguous at best.

5.2. Influence of the Inner Rotation Curve

The FIRE-2 galaxies are consistently baryon-dominated in their centers, with a slow-rising circular velocity in the inner DM component compared with a very sharply rising baryonic component. They hence produce relatively short bars, since the region where the overall rotation curve is rising, permitting swing amplification to operate, is relatively small. The subdominant DM component also leads to the formation of ellipsoidal bars (E. Athanassoula 2002; E. Athanassoula & A. Misiriotis 2002; I. Berentzen et al. 2006). Conversely, a larger DM fraction in the center at fixed stellar surface density can permit the formation of the longer, more rectangular bars apparent in simulations that form this type of galaxy in their halos (E. Athanassoula & A. Misiriotis 2002).

Another test for the relative influence of the central mass distribution comes from additional simulations in the FIRE-2 suite that include CR physics. These "CR-run" simulations use the same initial conditions as those in our study but form less massive disks in the same DM halos, since the CRs help moderate star formation but are otherwise not expected to influence bar formation (P. F. Hopkins et al. 2023). A bar does form in the CR version of m12b, m12b-CR, which has a similar inner circular velocity profile as the suite of galaxies without CRs: the stellar circular velocity peaks at the center ($V_{c,\rm max} = 248\,{\rm km\,s^{-1}}$ at $R_{\rm max} = 1.0$ kpc) and dominates over the slow-rising DM circular velocity up to a radius of $r \leqslant 6$ kpc. The stellar disk in m12b-CR is also kinematically colder than in the other CR-run galaxies, which favors bar formation (Section 4.2.2). The less massive m12f-CR fails to satisfy our bar criteria, as it does not maintain $A_2/A_0 > 0.1$ for long enough. The other CR-run galaxies (m12f-CR, m12c-CR, m12w-CR, and m12m-CR) are all less massive and have slow-rising DM rotation curves that peak at larger radii ($150 < V_{c,\rm max}/({\rm km\,s^{-1}}) < 200$ and $10 < R_{\rm max}/({\rm kpc}) < 22$); none of them form bars. Therefore, differences in rotation curves alone cannot fully explain our results.

5.3. The Impact of Stellar Feedback on Bar Formation

The bars in FIRE-2 galaxies exhibit periodic oscillations in the bar strength, A_2/A_0, at a wide range of frequencies within the same system. The overall bar strength varies on long timescales of more than a gigayear in the longest-lived bars, sometimes leading to intervals spent below the cutoff of 0.1 that we use to define a bar (Figure 4). At shorter timescales of about 0.1 Gyr, the bar strength and length (in the sense of the region in which $A_2/A_0 > 0.1$) also oscillates. This timescale is consistent with the timescale of "breathing modes" initiated by cycles of star formation and feedback, similar to the process

that can create cores in dwarf galaxies (S. Mashchenko et al. 2006; A. Pontzen & F. Governato 2012). Just as these relatively small but repetitive fluctuations in the potential can induce large-scale changes in the inner DM distribution, so they can also suppress bar formation, since the timescale of the breathing modes is comparable to the orbital period of the radial orbits needed to sustain the bar (both are essentially the dynamical time). Recent numerical experiments by M. D. Weinberg (2024) have shown that stochastic variations in the potential of the inner galaxy do not have to be very large to significantly change the eccentricity of stellar orbits caught at apocenter, thereby repeatedly disrupting the bar as it forms. M. D. Weinberg (2024) further shows that the characteristic frequency of the stochasticity needs to be only broadly consistent with the dynamical time to be effective at disrupting the bar. We believe this mechanism leads to the short-period oscillations seen in the FIRE-2 bars and suppresses strong bar formation. This explanation is tentative, since we have not yet confirmed that their model of the stochastic fluctuations is consistent with the process in our simulations. We aim to demonstrate this quantitatively in a future paper.

The significant role of stellar feedback in suppressing bar formation leads to several important implications. First, it implies that the bar length and strength should be anticorrelated with the star formation rate or gas fraction in the inner galaxy, as shown for our simulated bars in Figures 12 and 13. In other words, we do not expect bars to coincide with periods in which the star formation rate fluctuates significantly, consistent with the results of J. Neumann et al. (2020), or to be common in gas-rich galaxies, consistent with K. L. Masters et al. (2012) and A. Fraser-McKelvie et al. (2020). Second, it implies that simulations that do not account for this process, either by ignoring stellar feedback entirely (as in collisionless *N*-body simulations, but also those that include gas but not star formation, such as E. Athanassoula et al. 2013) or implementing it in a way that does not produce these small-scale fluctuations in the potential, as in Auriga (F. Fragkoudi et al. 2021), EAGLE (M. K. Cavanagh et al. 2022), and Illustris/IllustrisTNG (D. Zhao et al. 2020), are likely probing the upper limit of the strength of the bar instability in MW-mass galaxies.

An important caveat to this discussion is that the FIRE-2 galaxies do not include a model for feedback from a central supermassive black hole, which can in principle regulate star formation in the inner galaxy by lowering the gas fraction (J. Mercedes-Feliz et al. 2023; S. Wellons et al. 2023). Indeed, the FIRE-2 galaxies appear to have a somewhat higher star formation rate at $z_r \sim 0$ than the MW, although this conclusion depends somewhat on which measurements of the MW's star formation rate are used for the comparison (P. J. Gandhi et al. 2022). *Simulations* in which a subgrid AGN model does have this effect should therefore form longer and stronger bars; however, the efficiency of AGNs in removing gas from galaxy centers at this mass scale is *observationally* difficult to constrain, thanks to the complexity of the multiphase gas (e.g., A. C. Fabian 2012; C. M. Harrison 2017; R. Morganti 2017; A. J. Richings et al. 2021; S. Wellons et al. 2023). The FIRE-3 suite does include a model for BH formation and feedback; however, it also includes multiple other changes to other physical prescriptions that prevent apples-to-apples comparisons, especially since the net effect is to lower the total stellar masses of the galaxies by a factor of a few relative to FIRE-2 (P. F. Hopkins et al. 2023), which in turn changes the predisposition of the galaxies to form bars by lowering their surface density (as we found with the CR suite). Bars are also thought to funnel material toward a central BH (e.g., P. F. Hopkins & E. Quataert 2011), altering the mass accretion rate and making this a deeply nonlinear relationship. We thus defer a detailed study of the impact of introducing a BH feedback model on simulated bars to future work.

Another noteworthy aspect of bar formation is whether there exists a connection between the bar strength and the disk formation timescale (S. Khoperskov et al. 2024). We do not observe such a correlation between bar strengths at $z_r = 0$ and the lookback time of the Early Disk Era (see F. McCluskey et al. 2024) for the 13 galaxies in the FIRE-2 sample in the bar strength range $0.0 < A_2/A_0 < 0.2$. Two of the earliest-settling disks in the FIRE-2 sample (m12m and Romeo) form bars that are transient and do not last until $z_r = 0$.

6. Summary

In this work, we use the 13 MW-mass galaxies from the FIRE-2 zoom-in cosmological hydrodynamical simulations (P. F. Hopkins et al. 2018) to study bar formation and destruction in a complex cosmological environment with realistic star formation histories and feedback. Here, we summarize our main findings.

How bars form in FIRE-2 galaxies. We define an asymmetric instability to be a bar if the bar strength $A_2/A_0 > 0.1$ and the bar phase ϕ_2 is constant within $\pm 5°$ within the bar length for at least ∼two bar rotations. We find that in the FIRE-2 simulations, 8 out of 13 galaxies form bars at some point in their evolution. Not all are barred at $z_r = 0$. We consider 3 of these bars (m12f, m12b, and m12r) to result primarily from an interaction with a massive satellite, 4 (m12m, m12c, Remus, and Romeo) to arise from the internal evolution of the disk in the absence of any strong tidal forces, and 1 (m12w) to be due to the rapid evacuation of gas from the central few kiloparsecs. While the bars triggered by tidal interactions can form in slightly more dispersion-supported systems, the bars arising from internal evolution preferentially form in the most strongly rotation-supported, and therefore most kinematically cold, systems in our sample, and bars induced by tides last longer in colder systems (Section 4.2.2).

How bars do NOT form in FIRE-2 galaxies. Disk instabilities like bars and spiral arms arise in galaxies in the physical Universe either due to gravitational instabilities in the disk or due to satellite interactions or flyby events or a combination of both. Their origin in our simulations is likewise physical and is not due to Poisson noise, as is sometimes observed for bars forming in constrained galaxy simulations at lower resolution (J. Dubinski et al. 2009). At FIRE-2 resolution, the *N*-body relaxation timescale for the region of interest is longer than a Hubble time.

Galaxies without bars. 5 of the 13 galaxies in the FIRE-2 sample (m12i, Thelma, Louise, Romulus, and Juliet) either do not form a bar at all or show only small increases in A_2/A_0 for short intervals. The underlying reason in most cases is that the galaxy is too kinematically hot in the inner region, either because it hosts a large dispersion-supported central bulge (Louise, Juliet, and Romulus) or because it has a large number of satellite interactions that disturb and heat its disk (Thelma and m12i).

Bar characteristics. The bars that form in the FIRE-2 MW-mass galaxies have peak dipolar amplitudes A_2/A_0 in the range

0.1–0.2, lengths 1.4–3.7 kpc, and pattern speeds 36–97 km s^{-1} kpc^{-1} (Table 3). The corotation radius tends to be much larger than the bar length in most cases, so by the traditional $\mathcal{R}$ measure, the bars in FIRE-2 would be considered "slow" ($0.15 < a_s/R_{co} < 0.59$), although their pattern speeds are not intrinsically low. However, directly comparing the $\mathcal{R}$ measure of the bars in FIRE-2 with that of bars from observations (where the fast bars have $\mathcal{R} < 1.4$) is likely problematic, as most of the bars studied in observations are stronger and very different from the bars that we study here (E. M. Corsini 2011; J. A. L. Aguerri et al. 2015). In contrast, in a recent study, T. Geron et al. (2023) measured $\mathcal{R}$ for a galaxy sample of weak and strong bars to find that 62% of their bars are slow. Ideally, we need to compare $\mathcal{R}$ for similar types of bars in observations and in simulations. The lifetimes of the FIRE-2 bars range very widely: there are galaxies that host a bar for nearly their entire existence (m12b) once the disk settles, those that form a bar only in the last ∼500 Myr (m12w), and nearly everything in between (Table 2). Our bar properties are measured directly from the simulation particles, not from synthetic observations, and therefore we caution against their direct comparison to observational measurements, since the effects of light-weighting, extinction, projection, and observational selection have not been accounted for. We plan to consider the *observed* properties of the simulated bars in future work.

Future observational surveys will play an imperative role in the study of the formation of stellar bars and their properties across different redshifts. For a better understanding of bar formation and bar dissolution in a cosmological context, further study on the dynamical interactions between the bar, the stellar and gaseous disks, the surrounding DM halo, and the external satellite interactions is crucial.

Acknowledgments

This work was facilitated by the Pre-Doctoral Program of the Center for Computational Astrophysics at the Flatiron Institute; analysis was carried out on resources maintained by the Scientific Computing Core. The Flatiron Institute is supported by the Simons Foundation.

S.A. is grateful to the Simons Foundation for the support during the Pre-Doctoral Program from 2021 February to 2021 June.

Support for S.P. was provided by NASA through the NASA Hubble Fellowship grant #HST-HF2-51466.001-A awarded by the Space Telescope Science Institute, which is operated by the Association of Universities for Research in Astronomy, Incorporated, under NASA contract NAS5-26555. This work was supported by a research grant (VIL53081) from VILLUM FONDEN.

R.E.S. gratefully acknowledges support from the Simons Foundation as well as from NSF grant AST-2007232 and NASA grant 19-ATP19-0068.

Support for P.F.H. was provided by NSF Research Grants 1911233, 20009234, and 2108318, NSF CAREER grant 1455342, and NASA grants 80NSSC18K0562 and HST-AR-15800.

A.W. received support from: NSF via CAREER award AST-2045928 and grant AST-2107772; NASA ATP grant 80NSSC20K0513; and HST grants AR-15809, GO-15902, and GO-16273 from STScI.

E.C.C acknowledges the support for this work provided by NASA through the NASA Hubble Fellowship Program grant HST-HF2-51502 awarded by the Space Telescope Science Institute, which is operated by the Association of Universities for Research in Astronomy, Inc., for NASA, under contract NAS5-26555.

Numerical calculations were run on allocations AST21010 and AST20016, supported by the NSF and TACC, and NASA HEC SMD-16-7592.

Data Availability

The FIRE-2 simulations are publicly available (A. Wetzel et al. 2023) at http://flathub.flatironinstitute.org/fire. Additional FIRE simulation data are available at https://fire.northwestern.edu/data. A public version of the GIZMO code is available at http://www.tapir.caltech.edu/~phopkins/Site/GIZMO.html.

Software: astropy (Astropy Collaboration et al. 2013, 2018, 2022), gizmo analysis (A. Wetzel & S. Garrison-Kimmel 2020b), halo analysis (A. Wetzel & S. Garrison-Kimmel 2020a), AGAMA (E. Vasiliev 2019), photutils (L. Bradley et al. 2020).

Appendix A
Measurement of Bar Length

We estimate the bar lengths in the FIRE-2 barred galaxies using four different methods that are frequently used in the literature (J. A. L. Aguerri et al. 2000; E. Athanassoula & A. Misiriotis 2002; P. Erwin 2018). We also discuss how some of the methods are more suitable for certain types of bars than others and how the following methods perform for bar length estimation in the FIRE-2 galaxies.

1. Method 1: fitting elliptical isophotes in the bar region.
2. Method 2: using the bar strength distribution (A_2/A_0) as a function of disk radius.
3. Method 3: from the difference in surface densities between the bar major axis and the minor axis in the disk plane.
4. Method 4: from decomposition of the stellar surface density into Fourier modes (from J. A. L. Aguerri et al. 2000).

In Figure 14, we present examples of the above four methods for estimating bar length in m12f close to its peak bar strength. We show the fitted elliptical isophotes on the face-on density distribution (panel (a)) that is used to determine the PA (the magenta curve in panel (d)) and ellipticity (the dark green curve in panel (d)) as a function of disk radius. Panel (b) shows the bar length estimation using surface densities along the bar major axis and the minor axis. Panel (c) shows how we estimate the bar length using bar strength profile A_2/A_0 as a function of the disk radius R. Panel (e) shows the method using bar and interbar intensities (Method 4). The blue dashed vertical lines in all panels mark the bar length of m12f using different methods.

In the first method, we fit the bar in m12f with elliptical isophotes (see panel (a) in Figure 14), using the Python package *photutils* (L. Bradley et al. 2020) to find the PA and the ellipticity profile as a function of the disk radius (see panel (d) in Figure 14). We define a central bar region with an upper bound of radius set by the 20% decrease in the peak ellipticity

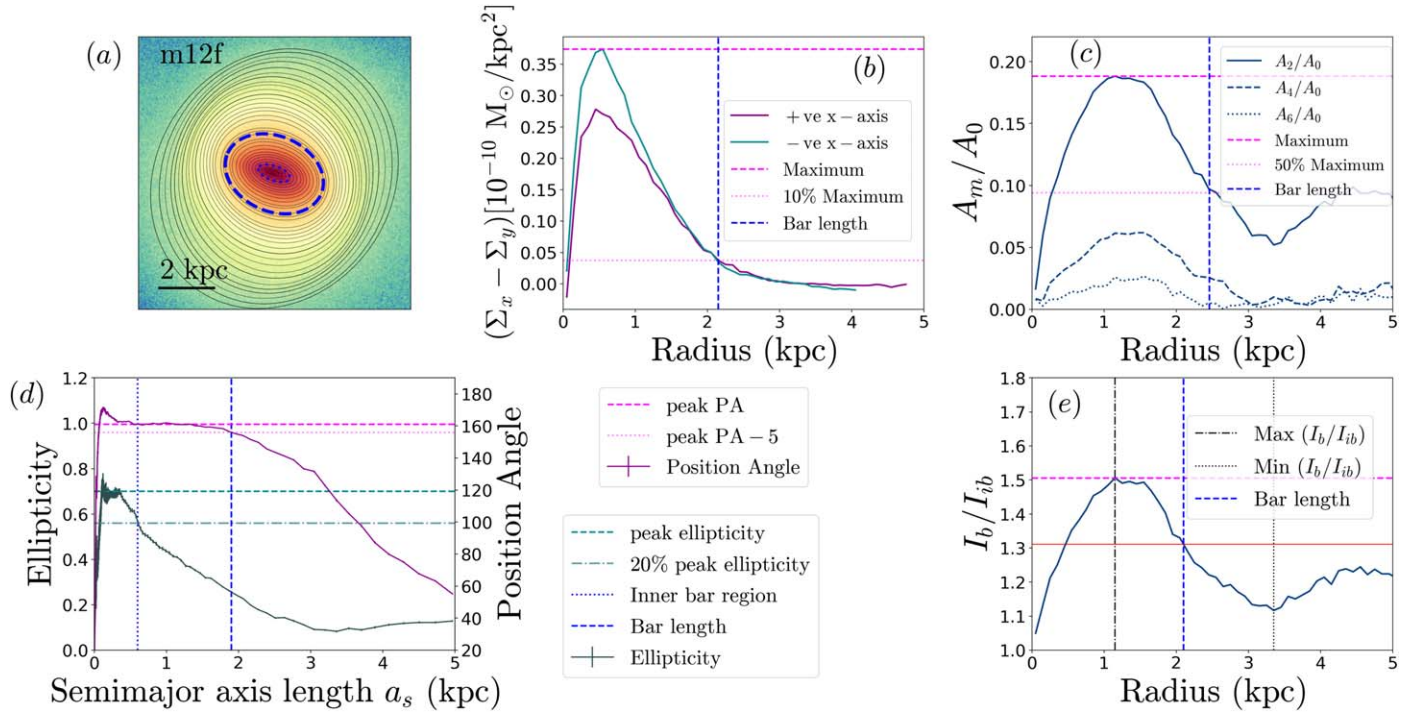

Figure 14. Estimation of bar lengths in the FIRE-2 galaxies using four methods. Method 1: panels (a) and (d) show the ellipse fitting method. The central bar region is chosen within the radius where there is a 20% decrease in the peak ellipticity value (marked with a blue dotted vertical line) and the corresponding PA is marked with a dashed magenta horizontal line. A deviation of ±5° in PA marks the edge of the bar/bar length (the blue dashed vertical line). Method 2: in panel (b), the difference in surface density Σ_x along the bar axis (x-axis) and Σ_y perpendicular to the bar axis (y-axis) is used to estimate the bar length at 10% of the peak value of $(\Sigma_x - \Sigma_y)$ (marked with the blue dashed line). The dissimilarity in $(\Sigma_x - \Sigma_y)$ along the positive and negative x-axis shows a slight asymmetry in the distribution, although the bar length estimate is the same for both. Method 3: the bar length is measured from the 50% decrease in bar strength in panel (c) (also marked with a blue dashed line). Method 4: in panel (e), the bar length is measured (marked with a blue dashed vertical line) from the ratio of the stellar density in the bar and the interbar region I_b/I_{ib} (from J. A. L. Aguerri et al. 2000). The radius of maximum I_b/I_{ib} is marked with a black dashed vertical line and the minimum is marked with a black dotted vertical line.

(the vertical blue dotted line in panel (d) in Figure 14). We define the bar length (the blue dashed vertical line in panel (d)) to be the radius at which the PA (magenta curve) changes by ±5° from its value at the edge of the central bar region (the blue dotted vertical line in panel (d)). The bars in m12f and other FIRE-2 galaxies are more round and do not show a sharp change in PA. The bars have the peak ellipticity close to the center ($R < 1$ kpc), with a gradual decrease of ellipticity away from the peak (see the dark green line of ellipticity in Figure 14). We therefore do not expect to find sharp changes in the PA and ellipticity at the edges of the bars, as is typically observed for rectangular/boxy-edge bars in studies with N-body simulations or in observations.

In the second method (panel (c) in Figure 14), we estimate the bar length at the radius where the bar strength A_2/A_0 drops to 50% of its peak value (see the blue vertical line in panel (c)).

In the third method (panel (b) in Figure 14), we estimate the bar length from the difference in surface density along the bar major axis (x-axis) and along the bar minor axis (y-axis) $(\Sigma_x - \Sigma_y)$. The bar length (the blue vertical dashed line in panel (b)) is defined to be the radius at which $(\Sigma_x - \Sigma_y)$ decreases by 80% of the peak value (the magenta dotted horizontal line).

In the fourth method (panel (e) in Figure 14), we use the ratio of the density contrast in the bar (I_b) and the interbar (I_{ib}) region, first introduced by K. Ohta et al. (1990) and redefined in J. A. L. Aguerri et al. (2000), where the authors defined the bar region as follows:

$$I_b/I_{ib} > \frac{(I_b/I_{ib})_{\max} - (I_b/I_{ib})_{\min}}{2} + (I_b/I_{ib})_{\min}, \qquad \text{(A1)}$$

where $I_b = A_0 + A_2 + A_4 + A_6$, $I_{ib} = A_0 - A_2 + A_4 - A_6$, and A_m is the amplitude of the mth Fourier mode. Here we use the condition from J. A. L. Aguerri et al. (2000) to determine the bar length (the blue dashed vertical line in panel (e)).

We present the semimajor axis length a_s (or half bar length) of the bars estimated using the four methods, as well as the average a_s from the four methods, in Table 5.

The ellipse fitting/PA method yields the shortest bar lengths for the strongest bars in m12f and m12b, while for other galaxies, the method using the bar and interbar density contrast yields the shortest bar lengths. The largest estimate of bar length for m12f and m12b comes from the method using the bar strength profile (Method 2), while for other bars, the methods using surface density and using an ellipticity/PA

Table 5
Bar Semimajor Axis Length a_s Estimates Using Different Methods

Simulation	$z_{r,\mathrm{peak}}$	$a_{s,1}$ (kpc)	$a_{s,2}$ (kpc)	$a_{s,3}$ (kpc)	$a_{s,4}$ (kpc)	Average a_s (kpc)
(1)	(2)	(3)	(4)	(5)	(6)	(7)
m12f	0.064	1.4	2.1	2.0	1.97	1.86
m12b	0.046	1.6	1.96	1.85	1.77	1.79
m12m	0.084	1.62	1.5	1.68	1.32	1.53
Romeo	0.038	1.26	1.21	1.45	1.16	1.32
Remus	0.041	2.1	1.42	1.55	1.25	1.58
m12w	0.0	1.35	1.41	1.45	1.18	1.35
m12c	0.0016	1.5	1.27	1.4	0.90	1.27
m12r	0.061	0.95	0.77	0.85	0.66	0.81

Note. Column (1): simulation name. Column (2): redshift of maximum bar strength. Column (3): bar semimajor axis length a_s measured using ellipticity/PA (Method 1). Column (4): a_s measured using the bar strength profile (Method 2). Column (5): a_s measured using the difference in surface densities between the major and minor axes of the bar (Method 3). Column (6): a_s measured using the bar–interbar density contrast method of J. A. L. Aguerri et al. (2000), as discussed in Section 3.3 (Method 4). Column (7): average of all a_s measurements in columns (3)–(6).

estimate provide the largest bar length. We note the similarity between the nature of the ellipticity and PA profiles in the FIRE-2 galaxies and the model MD in E. Athanassoula & A. Misiriotis (2002). This is expected, given the structural resemblance of the FIRE-2 bars to the bars having a round shape in model MD in E. Athanassoula & A. Misiriotis (2002).

Appendix B
Bar Length Evolution

Estimating the bar length at different time intervals is essential for determining the orbital time $T_o = 2\pi r/V_c(r)$ at the edge of the bars. We estimate the bar lengths of the FIRE-2 galaxies at multiple time intervals to estimate the orbital time T_o (see Section 3.1 and Table 2). We show two examples of bar length estimation in the FIRE-2 galaxies m12b and m12f in Figure 15.

In Figure 15, we present the evolution of the bar length for m12b (left panels (a) and (b)) and m12f (right panels (c) and (d)), estimated with the bar and interbar intensity ratio I_b/I_{ib} from Section A. The bar in m12b grows steadily in length inside out for a long duration of 5.7 Gyr, while, the bar in m12f maintains almost a constant length when bar strength $A_2/A_0 > 0.1$ (see panel (c) in Figure 15). Panels (b) and (c) show the evolution of the bar strength ($m = 2$) and other even Fourier modes ($m = 4$ and $m = 6$), which are in phase with the evolution of the higher amplitude of the $m = 2$ mode. Some of the large fluctuations in the bar length are due to large perturbations in the disk as a result of mergers (indicated by the black vertical lines), but most of the mergers do not affect the bar length estimates.

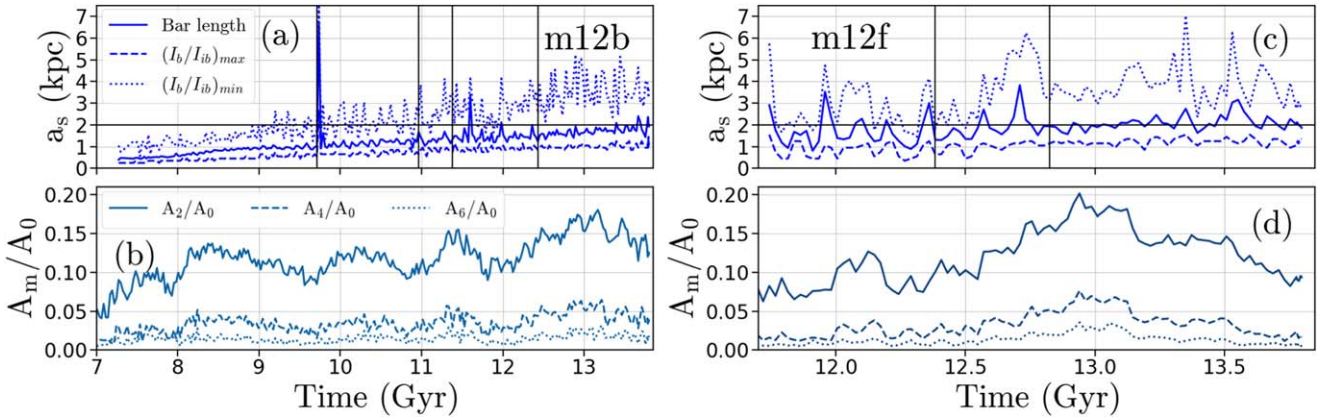

Figure 15. The evolution of the bar length (top panels) along with the evolution of the bar strength (bottom panels) in m12b (panels (a) and (b)) and in m12f (panels (c) and (d)). Top panels: the bar length (blue lines with dots), Max(I_b/I_{ib}) (dashed blue line), and Min(I_b/I_{ib}) (dotted blue line) are shown for m12b (panel (a)) and m12f (panel (c)) (J. A. L. Aguerri et al. 2000). The black vertical lines indicate the satellite mergers. Bottom panels: the bar strength A_2/A_0 (dark blue line), A_4/A_0 (dashed blue line), and A_6/A_0 (dotted blue line) are shown for m12b (panel (b)) and m12f (panel (d)). The maximum and minimum values of I_b/I_{ib} are for comparison. The large fluctuations in the bar length measurement are due to oscillations in the bar strength (see the bottom panels) and occasionally due to satellite mergers. The bar length in m12b grows to ∼2 kpc over a period of more than 5.7 Gyr, and in m12f the bar length is most stable at 2 kpc when the bar strength $A_2/A_0 > 0.1$.

Appendix C
Bar Pattern Speed Estimation with the TW Method

In this section, we present the TW method of the pattern-speed estimation of the bars in FIRE-2 in detail. The TW pattern speed is given by (M. R. Merrifield & K. Kuijken 1995)

$$\Omega_p \sin(i) = \frac{\int_{-\infty}^{\infty} \Sigma(X, Y) V_{\rm LOS}(X, Y) {\rm d}X}{\int_{-\infty}^{\infty} \Sigma(X, Y) X {\rm d}X} = \frac{\langle V \rangle}{\langle X \rangle}, \qquad \text{(C1)}$$

where X and Y are the sky coordinates and $\Sigma(X, Y)$ and $V_{\rm LOS}(X, Y)$ are the projected surface density and line-of-sight velocity on the sky plane. The numerator $\langle V \rangle$ and denominator $\langle X \rangle$ are weighted with the surface density $\Sigma(X, Y)$ along slits that are kept parallel to the kinematic PA of the disk, here the x-axis (see panels (a) and (c) in Figure 16).

The TW method works best when the galaxy disk is inclined by $\sim$45° to the line of sight of the observer and the angular separation between the bar PA and the kinematic PA (the x-axis marked with $\rm PA_K$ in panel (c) of Figure 16) of the disk is $\sim$41°. With the freedom to orient the simulation volume toward any line of sight, we fix the galaxy disk at the described orientation as shown in panels (a) and (b) of Figure 16. The TW method is based on the asymmetry about the $Y = 0$ line in the surface density and line-of-sight velocities (the red and blue curves in panels (d) and (e)) for slits that are off the x-axis (the red and blue slits in panel (a)). For each slit, we get a point in the $\langle V \rangle$ and $\langle X \rangle$ plot in panel (f). Ideally, all the points in panel (f) should lie on a straight line passing through the origin. Practically, all the points do not lie exactly on a straight line, as in panel (f), and we estimate the bar pattern speed from the slope of the fitted line. At peak bar strength, the bar pattern speed in m12f is $\Omega_p = 88\ {\rm km\ s^{-1}\ kpc^{-1}}$.

In the TW method, the disk is inclined by 45° to the line of sight and that decreases the bar length by $1/\sqrt{2}$ on disk reorientation. Hence, the TW method fails for short and weak bars in the FIRE-2 galaxies m12w, m12c, and m12r, even though their bar strength $A_2/A_0|_{\rm max} > 0.1$. For short and weak bars, we find that the surface density $\Sigma(X, Y)$ and line-of-sight velocity $V_{\rm LOS}(X, Y)$ profiles along the two extreme slits ($\pm$0.5 kpc) overlap and the asymmetry about $Y = 0$ in $\Sigma(X, Y)$ and $V_{\rm LOS}(X, Y)$ is lost. The similarity in $\Sigma(X, Y)$ and $V_{\rm LOS}(X, Y)$ for different slits leads to large errors in the estimation of $\langle X \rangle$ and $\langle V \rangle$ (Equation (C1)), which results in wrong estimates of the slope that is directly related to the pattern speed Ω_p.

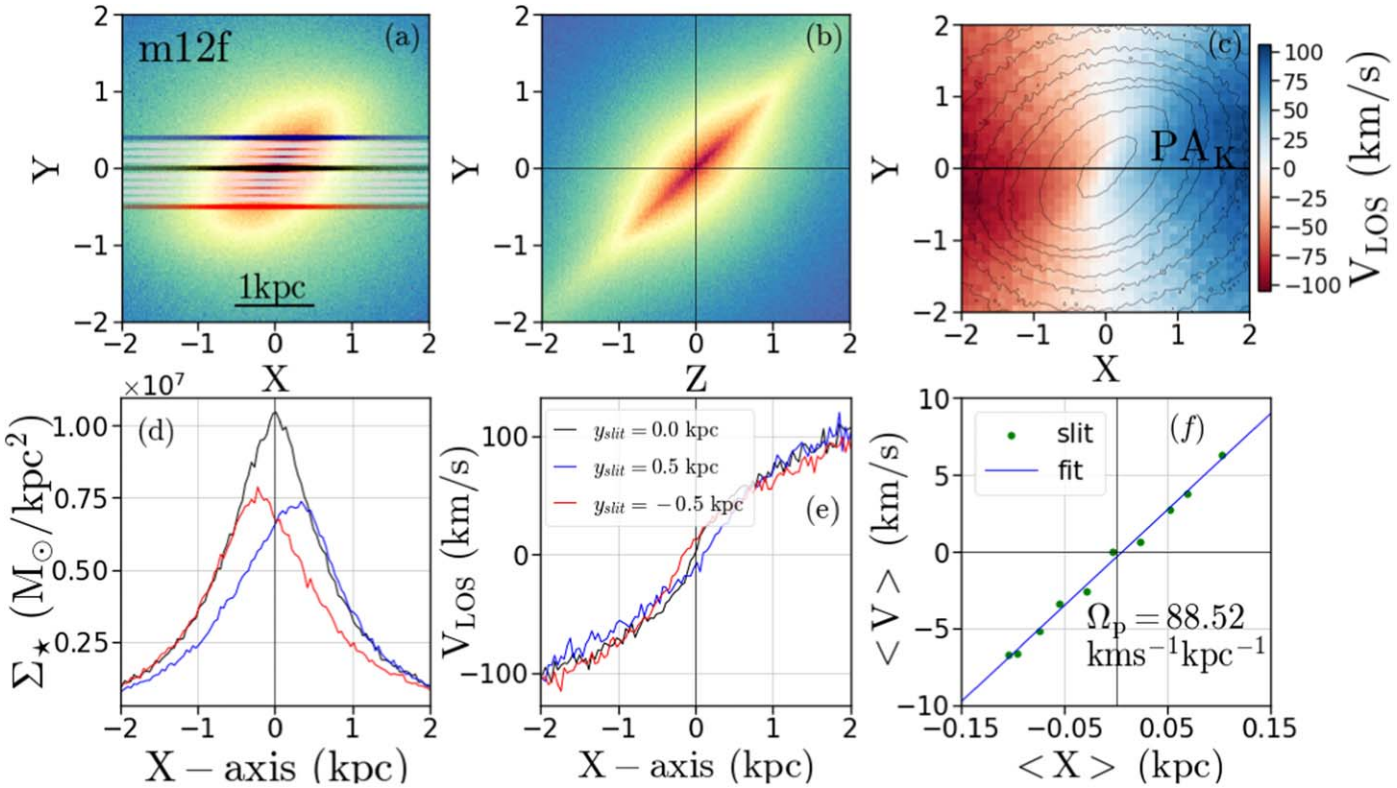

Figure 16. Application of the TW method to measure the bar pattern speed in m12f at its peak bar strength. In the TW method, slits are placed on the projected 2D density (panel (a)) and velocity map (panel (c)) of the galaxy m12f (at the maximum bar strength) along the kinematic PA ($\rm PA_K$) when the disk is oriented at a most suitable inclination of 45° from the line of sight (panel (b)) and the bar PA is $\sim$41° from the ($\rm PA_K$) of the disk. $\rm PA_K$ is kept along the x-axis (the black horizontal line in panel (c)). Panel (d) shows the surface density distribution and panel (e) shows line-of-sight velocity $V_{\rm LOS}$ distribution for the middle slit ($Y = 0$ kpc black curve) and the extreme slits ($Y = 0.5$ kpc (blue) and $Y = -0.5$ kpc (red)). The slope of $\langle V \rangle$ vs. $\langle X \rangle$ gives the bar pattern speed $\Omega_p = 88.5\ {\rm km\ s^{-1}\ kpc^{-1}}$ for m12f at the peak bar strength.

Appendix D
Direct Estimation of Bar Pattern Speed from Fourier Phase Angle

We present the direct measurement of the bar pattern speed in the FIRE-2 galaxies m12b, m12f, m12w, m12c, and Remus, which have nearly constant bar PA (within $\pm 5°$; similar to panel (c) of Figure 3) in the last 22 Myr of their evolution. We have 10 high-cadence snapshots ($0.0016 < z_r < 0$) with a time interval of 2.2 Myr between subsequent snapshots, for each of which we estimate the bar phase angle ϕ_2 (Equation (3)) in an annular ring of width 200 pc at their bar length $R = a_s$. We measure the bar length a_s using the bar and interbar density contrast (see Appendices A and B). The slope of $\phi_2|_{R=a_s}$ versus t is the bar pattern speed $\Omega_p = d\phi/dt$.

In Figure 17, we present the evolution of ϕ_2 with time for the bars in the galaxies m12b, m12f, m12w, m12c, and Remus. The slope of the fitted lines is the pattern speed $\Omega_p = d\phi/dt$. We show the bar pattern speed Ω_p (in kilometers per second per kiloparsec) at the bar length a_s for all the barred galaxies mentioned above. For m12b and m12f, we estimate the pattern speed at two radii close to bar length.

We compare the bar pattern-speed estimation by the direct method as described above with the pattern speed estimated using the TW method (see Section 3.4). In Figure 18, we present the comparison of bar pattern speeds in m12b, m12c, and Remus for the last 22 Myr. The pattern-speed estimation through the TW method matches with the direct method when the bar is long and strong. For example, for m12b, the pattern-speed estimates closely match the value of 89.47 km s^{-1} kpc^{-1} from the direct method, while for m12c and Remus the bar length is much shorter. When applying the TW method, an inclination of $\sim 45°$ of the galaxy plane with the line of sight makes the effective projected bar length further smaller, making it difficult to get a correct estimate of the slope for the $\langle X \rangle$ versus $\langle V_{\rm LOS} \rangle$ plot. In Figure 19, we present the median pattern-speed estimation of the bars in m12f, m12b, Romeo, and Remus for a range of snapshots where we otherwise cannot apply the direct estimation of pattern speed. We find that if either the bar length or the bar strength are low, the TW method cannot be applied. For example, for the bars in m12m, m12c, and m12w, the mean bar length is very short (2.49 kpc, 2.12 kpc, and 2.32 kpc, respectively) and the bar strength is also less (0.08, 0.11, and 0.15, respectively), and the inspection of the fits of $\langle X \rangle$ versus $\langle V_{\rm LOS} \rangle$ in the TW method are not reliable in these cases. Thus, the TW method does not give correct estimates of the pattern speeds for m12m, m12c, and m12w. We additionally compare our TW pattern-speed measurements with those obtained using the code patternSpeed.py from W. Dehnen et al. (2023), as shown in Figure 19. In the figure, these measurements are represented by blue triangles and error bars, all of which fall within the shaded 2σ region.

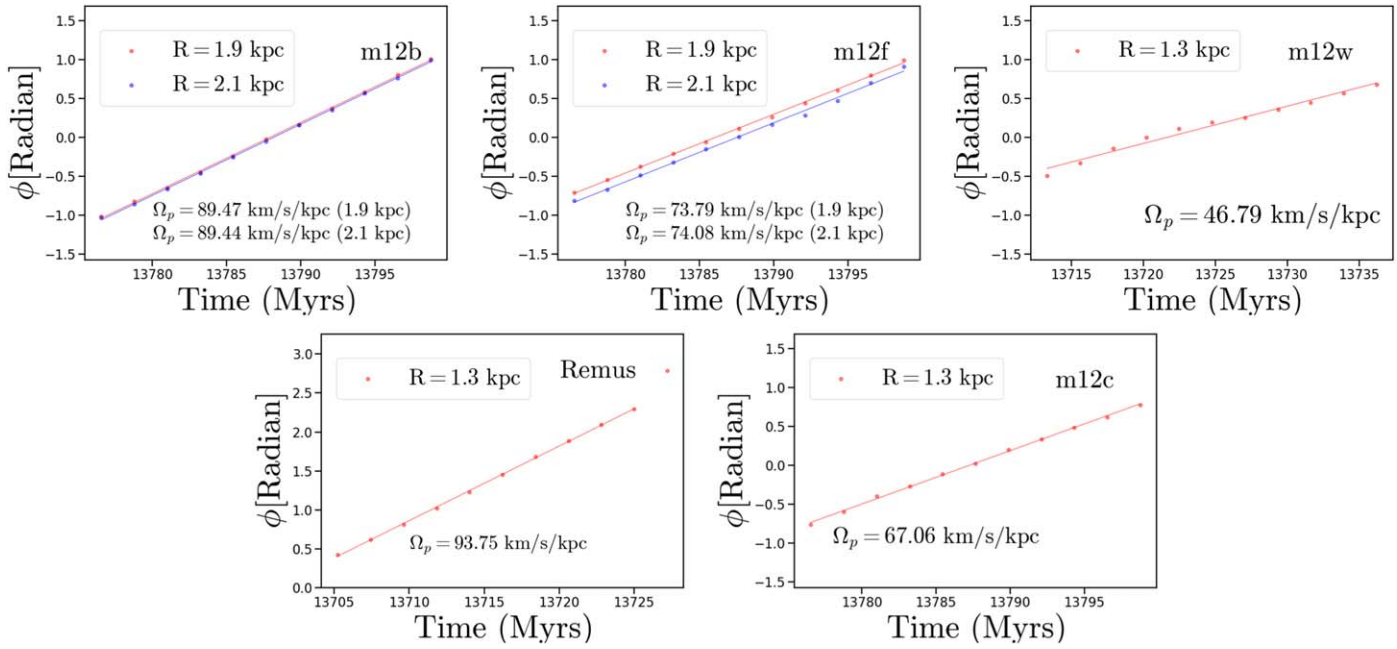

Figure 17. Direct measurement of pattern speed from high-cadence snapshots ($0.0016 < z_r < 0.0$) in the last 22 Myr of evolution of the FIRE-2 galaxies. We measure the pattern speed from the rate of change of the Fourier phase angle $\phi = \frac{1}{2}\tan^{-1}(b_2/a_2)$.

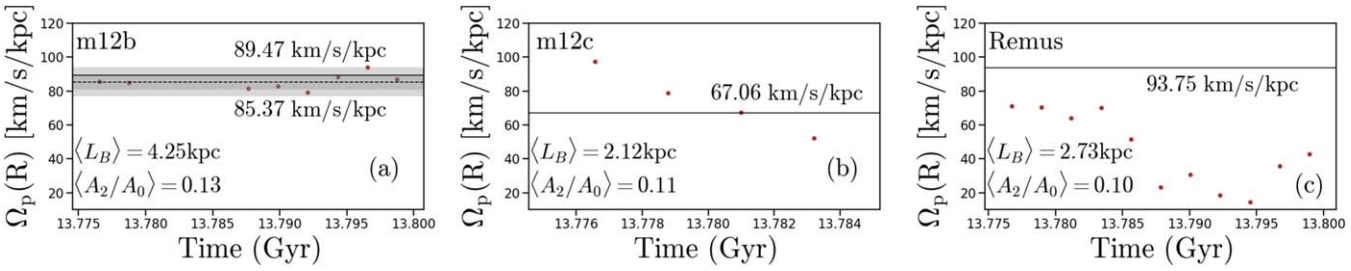

Figure 18. Comparison of bar pattern speed from direct measurement and using the TW method. The black horizontal line indicates the pattern speed estimated from the direct method and the brown dots represent that from the TW method at different times between redshift $0.0016 < z_r < 0.0$. The TW measurements at some snapshots do not give a good fit and are not plotted. $\langle A_2/A_0 \rangle$ and $\langle L_B \rangle$ are the mean bar strength and mean bar length for the same snapshot range. The bar length at each snapshot is measured using Method 4 in Section 3.3. The TW-method pattern speed matches with the direct-method pattern speed for the bars with high strength and longer length, like m12b, while it does not match for bars with lower strength and shorter length, like m12c and Remus.

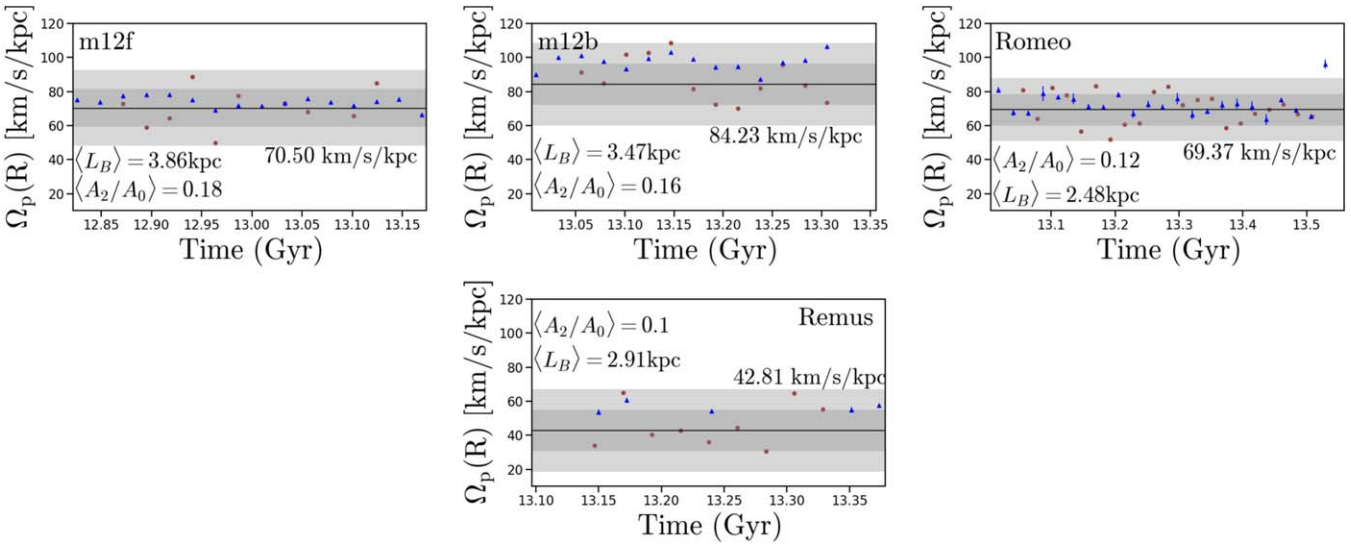

Figure 19. Median bar-pattern-speed measurement using the TW method from a range of time steps when the bar has maximum strength. The pattern-speed estimation through the TW method is possible for the bars in m12f, m12b, Romeo, and Remus with high strength and long length (see Figure 18). The black horizontal line indicates the median of the pattern speeds measured at each snapshot (brown dots) using the TW method, and the median value lies between 70 and 84 km s^{-1} kpc^{-1} for the three galaxies. The dark gray shades indicate the 1σ and 2σ regions. $\langle A_2/A_0 \rangle$ and $\langle L_B \rangle$ are the mean bar strength and mean bar length for the same snapshot range. The bar length at each snapshot is measured using Method 4 in Section 3.3 from J. A. L. Aguerri et al. (2000). The bar in Remus is shorter in length and weaker in strength compared to m12f, m12b, and Romeo, and hence the pattern-speed measurement is less reliable for Remus. The blue triangles, with blue error bars, in each panel show the pattern speed using the code patternSpeed.py from W. Dehnen et al. (2023). Some error bars are too small to be seen. We summarize the pattern-speed estimations for all the FIRE-2 galaxies in Table 3.

Appendix E
Evolution of Bar Pattern Speed in m12b

Figure 20 shows the evolution of the bar pattern speed Ω_p measured for m12b using the code patternSpeed.py (W. Dehnen et al. 2023). The bar pattern speed in m12b decreases steadily as the bar grows stronger, lengthens, and gains more stars that join the bar orbits. A decrease in the bar pattern speed indicates a loss of bar angular momentum (V. P. Debattista & J. A. Sellwood 2000), while the increase in bar length is due to the addition of more stars that can potentially increase the bar angular momentum. This complexity points to the challenge of disentangling the transfer of angular momentum between various components influenced by different processes in the galaxy's central region.

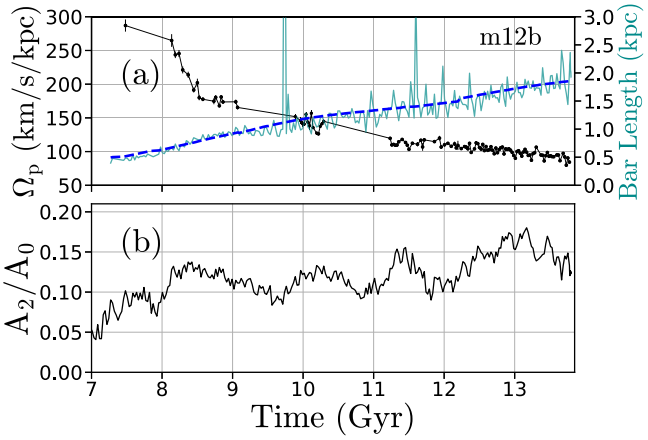

Figure 20. The pattern speed Ω_p decreases in m12b as the bar lengthens. Panel (a): evolution of the bar pattern speed (black circles) and evolution of the bar length (dark cyan line), along with the smoothed bar length (blue dashed line). Panel (b): evolution of bar strength in m12b.

Appendix F
Use of Tidal Index to Search for Satellites

We investigate the FIRE-2 galaxy satellites that can induce bar formation in the disk. Previously, many studies have looked into the formation of bars during galaxy encounters and flyby events (M. Lang et al. 2014; E. L. Łokas et al. 2014; E. L. Łokas 2018) and found that during the encounter of two galaxies, bars form in both galaxies having similar masses. Bars also form in the minor galaxy as it interacts with the more massive one (M. Lang et al. 2014). The bar formation depends on the orientation of the satellite galaxy orbit with respect to the direction of the total disk angular momentum of the more massive galaxy (E. L. Łokas 2018; M. K. Cavanagh & K. Bekki 2020).

To find the satellites, we investigate the merger trees of DM halos that are constructed using the codes ROCKSTAR (P. S. Behroozi et al. 2013a) and Consistent Trees (P. S. Behroozi et al. 2013b), which identify DM halos and trace their evolutionary history. We read the merger trees using the Python package *halo analysis* by A. Wetzel & S. Garrison-Kimmel (2020a), to find out the instantaneous satellite mass and distance from the host center of mass. We use the Python package *gizmo analysis* by A. Wetzel & S. Garrison-Kimmel (2020b) to read the stellar particle positions of the satellite galaxies and find the retrograde or prograde orientation of the satellite orbit. With the motivation of finding the satellites that may induce bar formation, we search for all the satellites ($M_{\rm total} > 10^7\ M_\odot$) in the FIRE-2 galaxies that undergo close tidal interactions with the host galaxy.

Figure 21 shows the tidal index Γ (Equation (7)) of the satellite galaxies in colored solid circles (color bar range: $-5 < \Gamma < 1$), along with their instantaneous DM halo mass ($M_{\rm sat}$) on the x-axis and their instantaneous distance ($D_{\rm H}$) from the host center of mass (y-axis), at each time snapshot between 6.6 and 13.7 Gyr. Note that Γ encapsulates the properties of the satellites as well as the host disk properties (see Section 4.1). In Figure 21, we present the different satellites in the FIRE-2 simulations, the maximum tidal index $\Gamma_{\rm max}$, and the corresponding time (in gigayears), for each simulation.

We find that the galaxies m12f, m12c, m12r, and Louise undergo the highest tidal index interaction after 10 Gyr of evolution when bar formation takes place, while the rest have their largest interaction in the early stages of evolution. One exception is m12b, where the bar forms early (∼8 Gyr). While studying bar formation in the FIRE-2 galaxies, we search for the satellite interactions close to the bar formation time. We investigate the high-Γ satellites that are close to the bar formation time and enlist the satellites and their properties in Table 4.

We test the effect of choosing a lower limit of Γ ($\Gamma < -2.45$). We find that such a choice will increase the number of satellite interactions, but the new interactions will not be leading the bar formation process in these simulations. For example, in the simulations m12f, m12b, and m12r, we still have the strongest satellites (shown in blue in Figure 6) playing the major role in bar formation. A lower cutoff of the tidal index will increase the number of satellite galaxies in m12m, m12w, m12c, Romeo, and Remus, which we present in Section 4.2, to be forming during the internal evolution of the disk. However, the new satellites (see Figure 22) do not have their pericenter passages or mergers within 10 dynamical times of the bar formation in these galaxies. Hence, selecting a lower limit of Γ does not seem to affect our results.

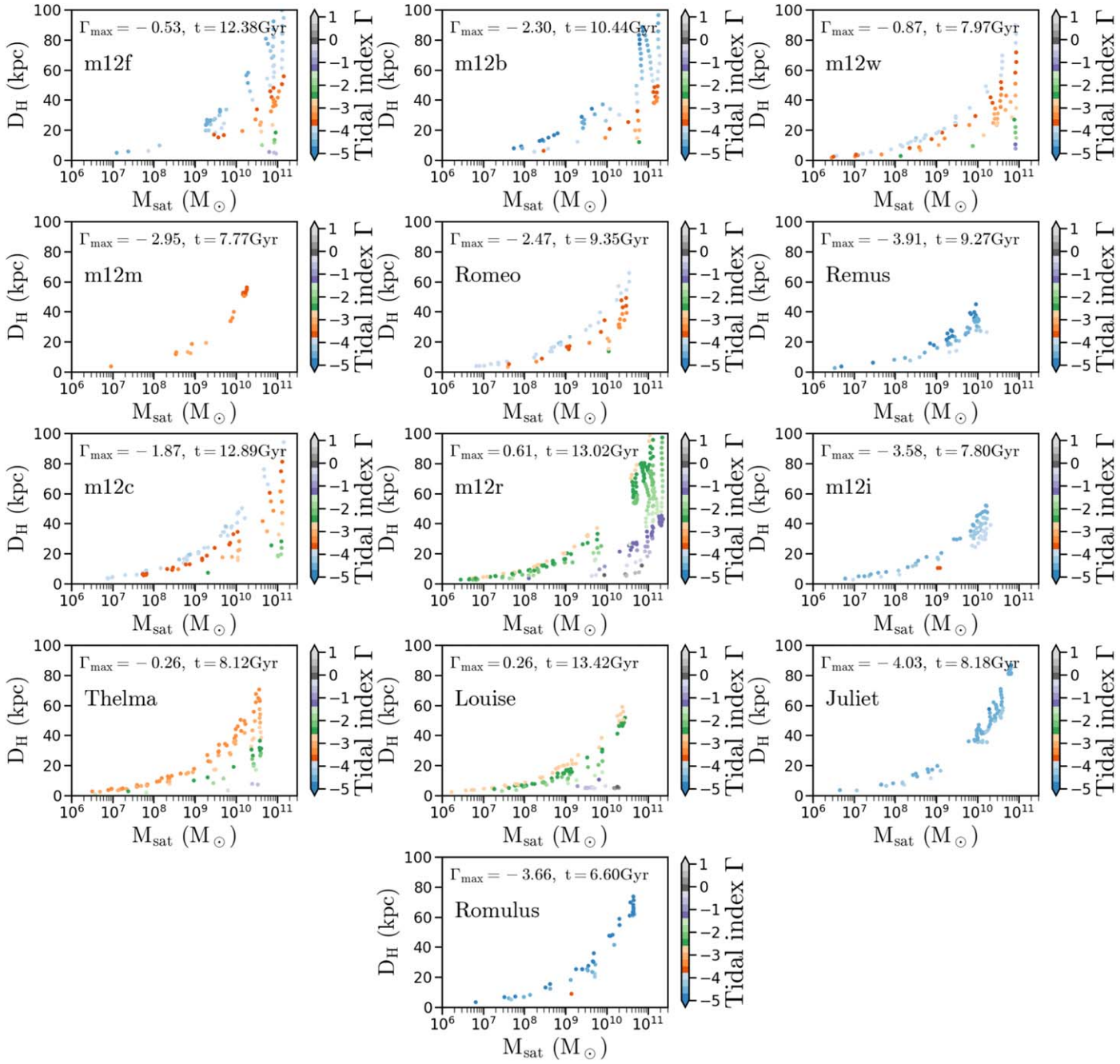

Figure 21. The tidal index Γ of all the satellites within a distance of 100 kpc from the host center, in the 13 FIRE-2 galaxies, for a time period of 6.6–13.7 Gyr of evolution. The points in each panel represent the satellites at each snapshot, with their instantaneous DM halo mass $M_{\rm sat}$ (in $M_\odot$) on the x-axis and the instantaneous total distance from the galaxy center $D_{\rm H}$ (in kiloparsecs) on the y-axis. The tidal index of the satellites for all the simulations, Γ, is shown with the color bar in the range $-5 < \Gamma < 1$. All satellites having $\Gamma \gtrsim -2.45$ may impart significant tidal force to the stellar disk. Often, the time of the maximum tidal impact by a satellite (i.e., the time of max Γ for each simulation) does not coincide with the time of bar formation.

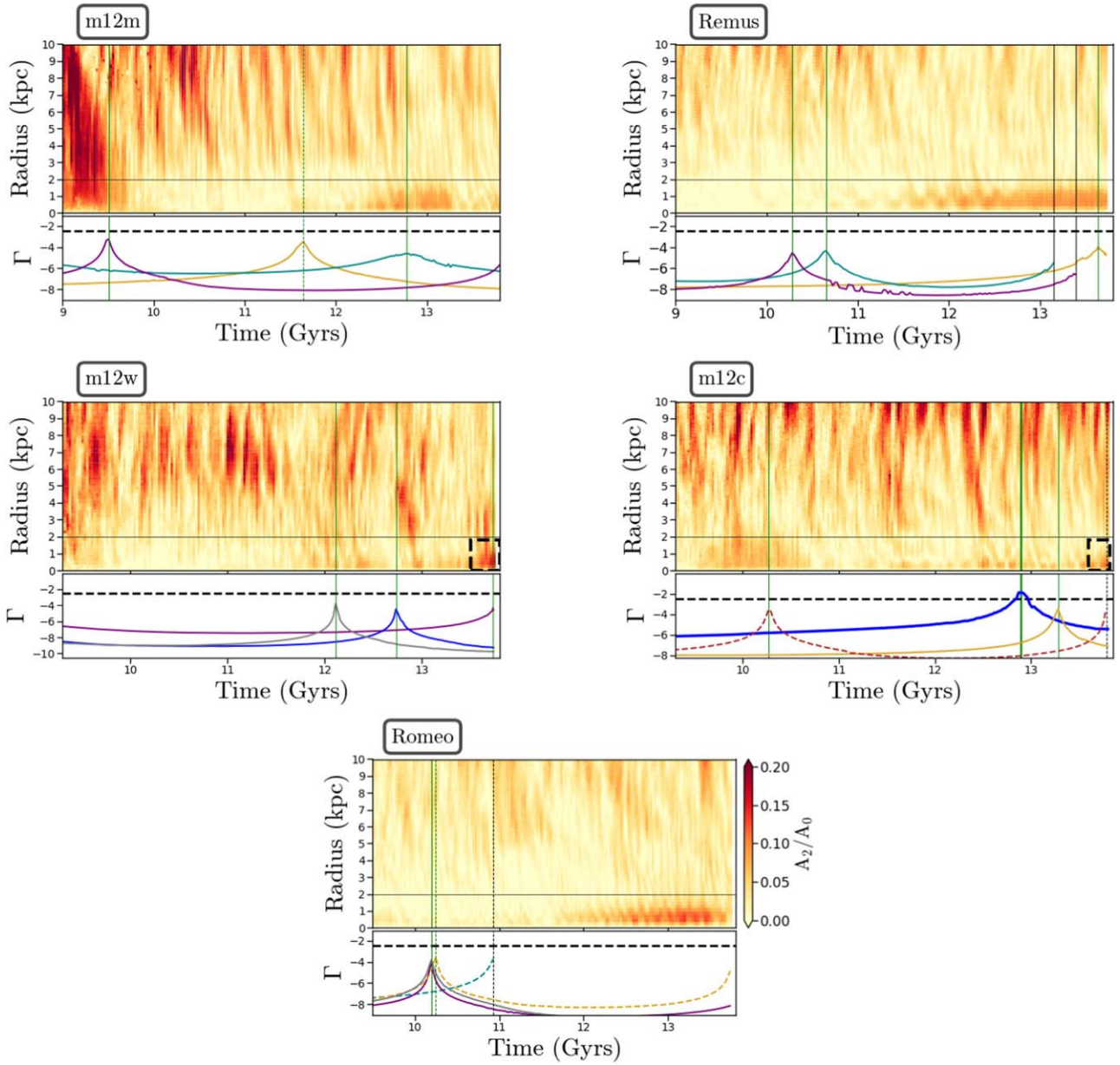

Figure 22. Low-tidal-index satellite interactions in m12m, Remus, m12c, m12w, and Romeo. Top panel for each simulation: evolution of the bar strength (shown with the color bar in the range $0.0 < A_2/A_0 < 0.2$). The dark reddish patch in the central region (radius <2 kpc) in the top panels shows the presence of the bar. Bottom panel for each simulation: evolution of the scaled tidal index Γ for the highest-tidal-index satellites close to bar formation. The colors and lines are the same as in Figure 6. We highlight the bar in m12w and m12c with the dashed rectangular boxes, as their duration in the disk is short. In the galaxies m12m, m12c, Remus, and Romeo, the satellite interactions are less impactful, with low tidal indices ($\Gamma \ll -2.45$). Even though the satellite in m12c has high Γ (>-2.45), it forms a bar after 22 dynamical times, too long to be causally related. Apart from the low tidal index, the time of maximum tidal impact of the satellites and the time of formation of the bar (around $A_2/A_0 \sim 0.1$) are well separated, such that satellite interactions cannot be the reason for the formation of the bars in these systems.

Appendix G
Rare Satellite Interactions in m12m, Remus, m12w, m12c, and Romeo

In this section, we present a few cases of satellite interactions in m12m, Remus, m12w, m12c, and Romeo that are either very weak with a low tidal index ($\Gamma < -2.45$) and/or the time of interaction with the host galaxy disk is a lot earlier than bar formation (more than 10 dynamical times), such that bar formation cannot be causally related to the satellite interaction (see Figure 22). We present the quantitative measurements of the highest-tidal-index satellite interactions in m12m, Remus, m12w, m12c, and Romeo in Table 4. Two of the strongest satellite interactions for Romeo are in retrograde and polar orbits ($\cos\theta_{\rm orbit} \sim -0.6$ and -0.04) and also more than 1.7 Gyr earlier (>50 dynamical times) than bar formation. The interactions in Remus are not only very weak, but the interactions happen either after the bar has already formed in the disk or more than 1.5 Gyr earlier (>40 dynamical times) than bar formation. The ineffectiveness of the satellite interactions is similar in the cases of m12m and m12w, as they impart weak tidal forces (with low $\Gamma = -3.45, -4.61$ for m12m and $\Gamma = -4.47$ for m12w) and/or the interactions are more than tens of dynamical times before the bar formation (33 $T_{\rm dyn}$ for m12m and 25 $T_{\rm dyn}$ for m12c). So the bars in these galaxies form as a result of the internal evolution of the disk.

Appendix H
Stellar Surface Density Profiles

We present the stellar surface density profile along the bar major axis and minor axis in m12f and m12b, at their peak bar strength, in Figure 23.

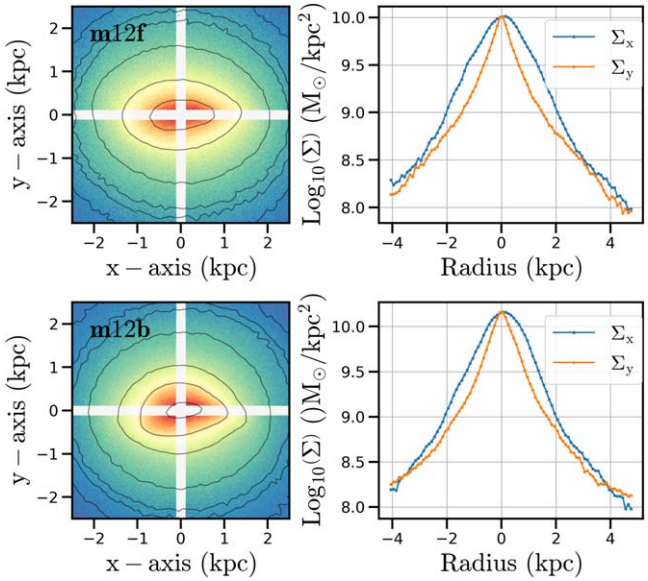

Figure 23. Stellar surface density profiles along the bar major axis and minor axis in m12f (top row) and m12b (bottom row) at the peak bar strength. The left column shows the face-on images of the central regions in m12f and m12b, with the slits (white) used to measure the surface density in the right column. In the right column, the surface density Σ_x (blue) is along the bar major axis, and Σ_y (orange) is along the bar minor axis.

Appendix I
Kinematic Coldness of Disks in FIRE-2

In this section, we present the history of the kinematic coldness of the stellar disks for the FIRE-2 barred galaxies (m12m, m12w, m12c, and Remus) in Figure 24 and the unbarred galaxies (Juliet, Thelma, and Romulus) having central bulges in Figure 25.

We note that among the barred galaxies, m12m, Remus, m12w, and m12c have similar kinematically cold inner disks ($r < 5$ kpc) at later stage of evolution (>11 Gyr), even though the outer disk is kinematically hotter for m12w and m12c compared to the colder disk in m12m and Remus. The kinematic coldness of the inner disk is important for the bar instability to grow. However, we also note that a kinematically hotter disk does not always guarantee stability against bar formation (A. Klypin et al. 2009; M. Aumer & J. Binney 2017; S. Ghosh et al. 2023), as seen for the bar formation in m12m and Remus, which have relatively hotter disks than m12f and m12b.

In Figure 25, both the disks in Juliet and Thelma appear to be kinematically hotter compared to the disk in Romulus, but none of them show a bar instability, probably due to the presence of a stellar bulge.

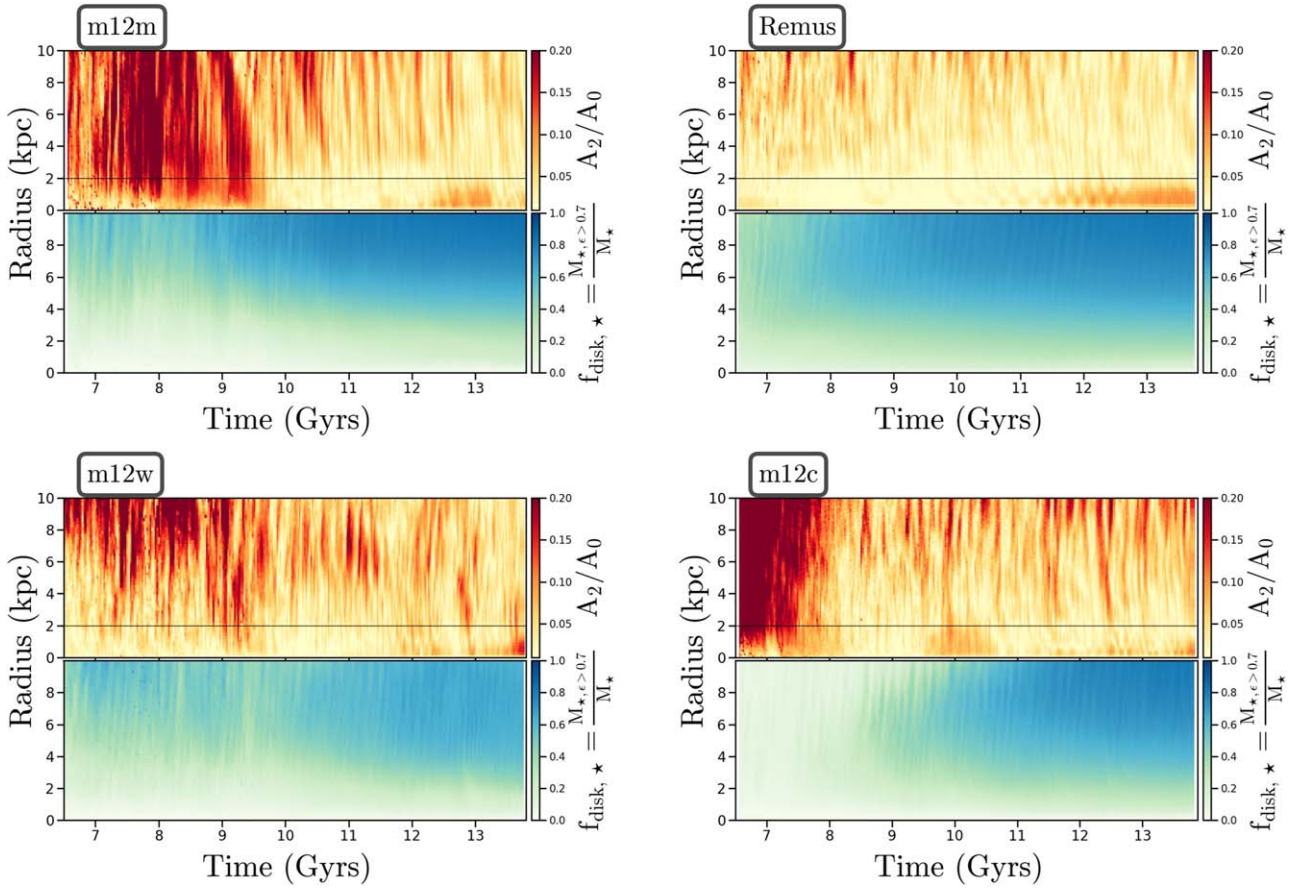

Figure 24. Weak bars and kinematic coldness of the stellar disk. The history of the bar strength (A_2/A_0) evolution (top panels for each simulation, with the color bar for bar strength: $0.0 < A_2/A_0 < 0.2$) along with the kinematic coldness parameter $f_{\rm disk}(r) = M_{\star,\epsilon\,>\,0.7}/M_\star$ of the stellar disk (bottom panels for each simulation, with color bar: $0.0 < f_{\rm disk} < 1.0$) for all the barred galaxies in FIRE-2 (the same as Figure 11). The bars in m12m and Remus form in kinematically hotter disks than m12b and m12f, during the internal evolution of the disks. m12w and m12c are short bars that arise in disks that are not so cold kinematically.

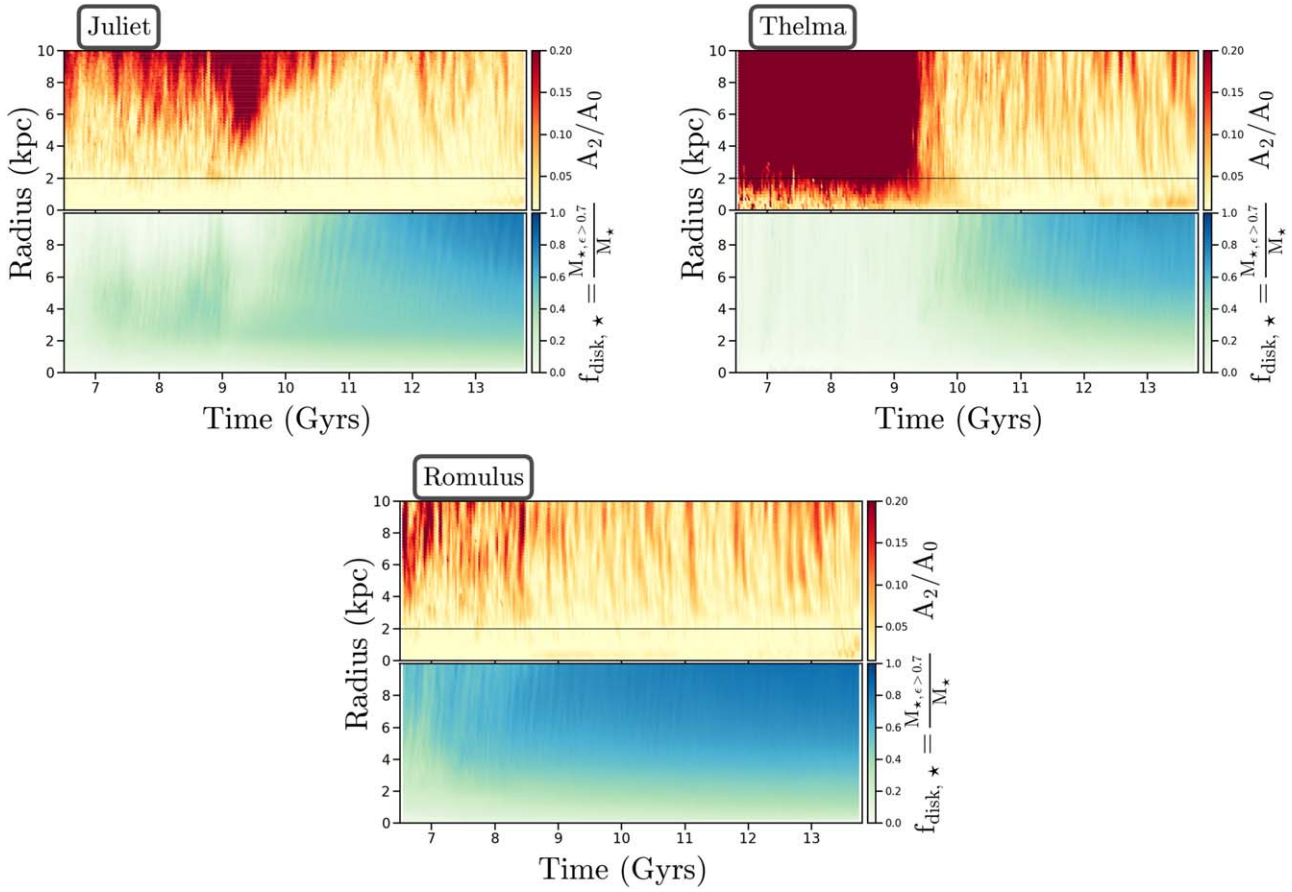

Figure 25. Unbarred galaxies and the kinematic hotness/coldness of their stellar disks. The colors and axes are the same as in Figure 11. Thelma is a failed bar with $A_2/A_0 < 0.1$. Juliet has a bulge at its center and a kinematically hot stellar disk. Romulus has a bulge at its center, but the outer stellar disk is relatively cold kinematically.

ORCID iDs

Sioree Ansar https://orcid.org/0000-0002-3353-6421
Sarah Pearson https://orcid.org/0000-0003-0256-5446
Robyn E. Sanderson https://orcid.org/0000-0003-3939-3297
Arpit Arora https://orcid.org/0000-0002-8354-7356
Philip F. Hopkins https://orcid.org/0000-0003-3729-1684
Andrew Wetzel https://orcid.org/0000-0003-0603-8942
Emily C. Cunningham https://orcid.org/0000-0002-6993-0826
Jamie Quinn https://orcid.org/0000-0001-6086-9873

References

Abadi, M. G., Navarro, J. F., Steinmetz, M., & Eke, V. R. 2003, ApJ, 597, 21
Aguerri, J. A. L. 1999, A&A, 351, 43
Aguerri, J. A. L., Méndez-Abreu, J., Falcón-Barroso, J., et al. 2015, A&A, 576, A102
Aguerri, J. A. L., Muñoz-Tuñón, C., Varela, A. M., & Prieto, M. 2000, A&A, 361, 841
Anglés-Alcázar, D., Quataert, E., Hopkins, P. F., et al. 2021, ApJ, 917, 53
Ansar, S., Kataria, S. K., & Das, M. 2023, MNRAS, 522, 2967
Arora, A., Sanderson, R., Regan, C., et al. 2024, ApJ, 977, 23
Arora, A., Sanderson, R. E., Panithanpaisal, N., et al. 2022, ApJ, 939, 2
Astropy Collaboration, Price-Whelan, A. M., Lim, P. L., et al. 2022, ApJ, 935, 167
Astropy Collaboration, Price-Whelan, A. M., Sipőcz, B. M., et al. 2018, AJ, 156, 123
Astropy Collaboration, Robitaille, T. P., Tollerud, E. J., et al. 2013, A&A, 558, A33
Athanassoula, E. 2002, ApJL, 569, L83
Athanassoula, E., Machado, R. E. G., & Rodionov, S. A. 2013, MNRAS, 429, 1949
Athanassoula, E., & Misiriotis, A. 2002, MNRAS, 330, 35
Aumer, M., & Binney, J. 2017, MNRAS, 470, 2113
Barazza, F. D., Jogee, S., & Marinova, I. 2008, ApJ, 675, 1194
Behroozi, P. S., Wechsler, R. H., & Wu, H.-Y. 2013a, ApJ, 762, 109
Behroozi, P. S., Wechsler, R. H., Wu, H.-Y., et al. 2013b, ApJ, 763, 18
Benincasa, S. M., Loebman, S. R., Wetzel, A., et al. 2020, MNRAS, 497, 3993
Berentzen, I., Shlosman, I., & Jogee, S. 2006, ApJ, 637, 582
Bovy, J., Leung, H. W., Hunt, J. A. S., et al. 2019, MNRAS, 490, 4740
Bradley, L., Sipőcz, B., Robitaille, T., et al. 2020, astropy/photutils: 1.0.1, v1.0.1, Zenodo, doi:10.5281/zenodo.4049061
Cavanagh, M. K., & Bekki, K. 2020, A&A, 641, A77
Cavanagh, M. K., Bekki, K., Groves, B. A., & Pfeffer, J. 2022, MNRAS, 510, 5164
Combes, F., & Sanders, R. H. 1981, A&A, 96, 164
Corsini, E. M. 2011, MSAIS, 18, 23
Debattista, V. P., Gonzalez, O. A., Sanderson, R. E., et al. 2019, MNRAS, 485, 5073
Debattista, V. P., Mayer, L., Carollo, C. M., et al. 2006, ApJ, 645, 209
Debattista, V. P., & Sellwood, J. A. 1998, ApJL, 493, L5
Debattista, V. P., & Sellwood, J. A. 2000, ApJ, 543, 704
Dehnen, W., Semczuk, M., & Schönrich, R. 2023, MNRAS, 518, 2712
Dubinski, J., Berentzen, I., & Shlosman, I. 2009, ApJ, 697, 293
Efstathiou, G., Lake, G., & Negroponte, J. 1982, MNRAS, 199, 1069
El-Badry, K., Quataert, E., Wetzel, A., et al. 2018, MNRAS, 473, 1930
El-Badry, K., Wetzel, A., Geha, M., et al. 2016, ApJ, 820, 131
Erwin, P. 2018, MNRAS, 474, 5372
Erwin, P., Debattista, V. P., & Anderson, S. R. 2023, MNRAS, 524, 3166
Fabian, A. C. 2012, ARA&A, 50, 455
Fragkoudi, F., Grand, R., Pakmor, R., et al. 2024, arXiv:2406.09453
Fragkoudi, F., Grand, R. J. J., Pakmor, R., et al. 2021, A&A, 650, L16
Fraser-McKelvie, A., Merrifield, M., Aragón-Salamanca, A., et al. 2020, MNRAS, 499, 1116

Fujii, M. S., Bédorf, J., Baba, J., & Portegies Zwart, S. 2018, MNRAS, 477, 1451
Gadotti, D. A. 2011, MNRAS, 415, 3308
Gandhi, P. J., Wetzel, A., Hopkins, P. F., et al. 2022, MNRAS, 516, 1941
Garrison-Kimmel, S., Hopkins, P. F., Wetzel, A., et al. 2018, MNRAS, 481, 4133
Garrison-Kimmel, S., Hopkins, P. F., Wetzel, A., et al. 2019a, MNRAS, 487, 1380
Garrison-Kimmel, S., Wetzel, A., Bullock, J. S., et al. 2017, MNRAS, 471, 1709
Garrison-Kimmel, S., Wetzel, A., Hopkins, P. F., et al. 2019b, MNRAS, 489, 4574
Gensior, J., Feldmann, R., Mayer, L., et al. 2023, MNRAS, 518, L63
Gerin, M., Combes, F., & Athanassoula, E. 1990, A&A, 230, 37
Geron, T., Smethurst, R. J., Lintott, C., et al. 2023, MNRAS, 521, 1775
Ghosh, S., & Di Matteo, P. 2024, A&A, 683, A100
Ghosh, S., Fragkoudi, F., Di Matteo, P., & Saha, K. 2023, A&A, 674, A128
Ghosh, S., Saha, K., Di Matteo, P., & Combes, F. 2021, MNRAS, 502, 3085
González-Alfonso, E., Pereira-Santaella, M., Fischer, J., et al. 2021, A&A, 645, A49
Grand, R. J. J., Fragkoudi, F., Gómez, F. A., et al. 2024, MNRAS, 532, 1814
Grand, R. J. J., Gómez, F. A., Marinacci, F., et al. 2017, MNRAS, 467, 179
Grion Filho, D., Johnston, K. V., Poggio, E., et al. 2021, MNRAS, 507, 2825
Guo, Y., Jogee, S., Finkelstein, S. L., et al. 2023, ApJL, 945, L10
Guo, Y., Jogee, S., Wise, E., et al. 2024, arXiv:2409.06100
Gurvich, A. B., Stern, J., Faucher-Giguère, C.-A., et al. 2023, MNRAS, 519, 2598
Guszejnov, D., Grudić, M. Y., Offner, S. S. R., et al. 2020, MNRAS, 492, 488
Harrison, C. M. 2017, NatAs, 1, 0165
Hohl, F. 1971, ApJ, 168, 343
Hopkins, P. F. 2015, MNRAS, 450, 53
Hopkins, P. F. 2017, arXiv:1712.01294
Hopkins, P. F., Gurvich, A. B., Shen, X., et al. 2023, MNRAS, 525, 2241
Hopkins, P. F., Narayanan, D., & Murray, N. 2013, MNRAS, 432, 2647
Hopkins, P. F., & Quataert, E. 2011, MNRAS, 415, 1027
Hopkins, P. F., Wetzel, A., Kereš, D., et al. 2018, MNRAS, 480, 800
Irodotou, D., Fragkoudi, F., Pakmor, R., et al. 2022, MNRAS, 513, 3768
Izquierdo-Villalba, D., Bonoli, S., Rosas-Guevara, Y., et al. 2022, MNRAS, 514, 1006
Julian, W. H., & Toomre, A. 1966, ApJ, 146, 810
Karachentsev, I. D., & Makarov, D. I. 1999, in IAU Symp. 186, Galaxy Interactions at Low and High Redshift, ed. J. E. Barnes & D. B. Sanders (Cambridge: Cambridge Univ. Press), 109
Khoperskov, S., Haywood, M., Di Matteo, P., Lehnert, M. D., & Combes, F. 2018, A&A, 609, A60
Khoperskov, S., Minchev, I., Steinmetz, M., et al. 2024, MNRAS, 533, 3975
Klypin, A., Valenzuela, O., Colín, P., & Quinn, T. 2009, MNRAS, 398, 1027
Kroupa, P. 2001, MNRAS, 322, 231
Lang, M., Holley-Bockelmann, K., & Sinha, M. 2014, ApJL, 790, L33
Lazar, A., Bullock, J. S., Boylan-Kolchin, M., et al. 2020, MNRAS, 497, 2393
Le Conte, Z. A., Gadotti, D. A., Ferreira, L., et al. 2024, MNRAS, 530, 1984
Leitherer, C., Schaerer, D., Goldader, J. D., et al. 1999, ApJS, 123, 3
Li, X., Shlosman, I., Heller, C., & Pfenniger, D. 2023, MNRAS, 526, 1972
Łokas, E. L. 2018, ApJ, 857, 6
Łokas, E. L. 2020, A&A, 634, A122
Łokas, E. L. 2021, A&A, 655, A97
Łokas, E. L., Athanassoula, E., Debattista, V. P., et al. 2014, MNRAS, 445, 1339
Łokas, E. L., Ebrová, I., del Pino, A., et al. 2016, ApJ, 826, 227
Lucey, M., Pearson, S., Hunt, J. A. S., et al. 2023, MNRAS, 520, 4779
Ma, X., Hopkins, P. F., Wetzel, A. R., et al. 2017, MNRAS, 467, 2430
Marioni, O. F., Abadi, M. G., Gottlöber, S., & Yepes, G. 2022, MNRAS, 511, 2423
Martinez-Valpuesta, I., Aguerri, J. A. L., González-García, A. C., Dalla Vecchia, C., & Stringer, M. 2017, MNRAS, 464, 1502
Mashchenko, S., Couchman, H. M. P., & Wadsley, J. 2006, Natur, 442, 539
Masters, K. L., Nichol, R. C., Haynes, M. P., et al. 2012, MNRAS, 424, 2180
Masters, K. L., Nichol, R. C., Hoyle, B., et al. 2011, MNRAS, 411, 2026
McCluskey, F., Wetzel, A., Loebman, S. R., Moreno, J., & Faucher-Giguere, C.-A. 2024, MNRAS, 527, 6926
Mercedes-Feliz, J., Anglés-Alcázar, D., Hayward, C. C., et al. 2023, MNRAS, 524, 3446
Merrifield, M. R., & Kuijken, K. 1995, MNRAS, 274, 933
Michel-Dansac, L., & Wozniak, H. 2006, A&A, 452, 97
Miwa, T., & Noguchi, M. 1998, ApJ, 499, 149
Morganti, R. 2017, FrASS, 4, 42
Neumann, J., Fragkoudi, F., Pérez, I., et al. 2020, A&A, 637, A56
Ohta, K., Hamabe, M., & Wakamatsu, K.-I. 1990, ApJ, 357, 71
Orr, M. E., Hayward, C. C., Hopkins, P. F., et al. 2018, MNRAS, 478, 3653
Orr, M. E., Hayward, C. C., Medling, A. M., et al. 2020, MNRAS, 496, 1620
Ostriker, J. P., & Peebles, P. J. E. 1973, ApJ, 186, 467
Pearson, S., Besla, G., Putman, M. E., et al. 2016, MNRAS, 459, 1827
Pessa, I., Schinnerer, E., Sanchez-Blazquez, P., et al. 2023, A&A, 673, A147
Pillepich, A., Springel, V., Nelson, D., et al. 2018, MNRAS, 473, 4077
Pontzen, A., & Governato, F. 2012, MNRAS, 421, 3464
Purcell, C. W., Bullock, J. S., Tollerud, E. J., Rocha, M., & Chakrabarti, S. 2011, Natur, 477, 301
Quillen, A. C., Minchev, I., Sharma, S., Qin, Y.-J., & Di Matteo, P. 2014, MNRAS, 437, 1284
Reddish, J., Kraljic, K., Petersen, M. S., et al. 2022, MNRAS, 512, 160
Richings, A. J., Faucher-Giguère, C.-A., & Stern, J. 2021, MNRAS, 503, 1568
Romeo, A. B., Agertz, O., & Renaud, F. 2023, MNRAS, 518, 1002
Rosas-Guevara, Y., Bonoli, S., Dotti, M., et al. 2022, MNRAS, 512, 5339
Roshan, M., Ghafourian, N., Kashfi, T., et al. 2021, MNRAS, 508, 926
Samuel, J., Wetzel, A., Tollerud, E., et al. 2020, MNRAS, 491, 1471
Sanders, J. L., Smith, L., & Evans, N. W. 2019, MNRAS, 488, 4552
Sanderson, R. E., Wetzel, A., Loebman, S., et al. 2020, ApJS, 246, 6
Santistevan, I. B., Wetzel, A., El-Badry, K., et al. 2020, MNRAS, 497, 747
Schaye, J., Crain, R. A., Bower, R. G., et al. 2015, MNRAS, 446, 521
Sellwood, J. A. 2014, RvMP, 86, 1
Sellwood, J. A., & Gerhard, O. 2020, MNRAS, 495, 3175
Sellwood, J. A., & Wilkinson, A. 1993, RPPh, 56, 173
Seo, W.-Y., Kim, W.-T., Kwak, S., et al. 2019, ApJ, 872, 5
Sheth, K., Vogel, S. N., Regan, M. W., Thornley, M. D., & Teuben, P. J. 2005, ApJ, 632, 217
Shlosman, I., Frank, J., & Begelman, M. C. 1989, Natur, 338, 45
Sun, J., Leroy, A. K., Schinnerer, E., et al. 2020, ApJL, 901, L8
Toomre, A. 1964, ApJ, 139, 1217
Toomre, A. 1981, in Proc. of the Advanced Study Institute, The Structure and Evolution of Normal Galaxies, ed. S. M. Fall & D. Lynden-Bell (Cambridge: Cambridge Univ. Press), 111
Tremaine, S., & Weinberg, M. D. 1984, ApJL, 282, L5
Trick, W. H. 2022, MNRAS, 509, 844
Trick, W. H., Fragkoudi, F., Hunt, J. A. S., Mackereth, J. T., & White, S. D. M. 2021, MNRAS, 500, 2645
Vasiliev, E. 2019, MNRAS, 482, 1525
Vogelsberger, M., Genel, S., Springel, V., et al. 2014a, MNRAS, 444, 1518
Vogelsberger, M., Genel, S., Springel, V., et al. 2014b, Natur, 509, 177
Wang, L., Dutton, A. A., Stinson, G. S., et al. 2015, MNRAS, 454, 83
Wegg, C., Gerhard, O., & Bieth, M. 2019, MNRAS, 485, 3296
Wegg, C., Gerhard, O., & Portail, M. 2015, MNRAS, 450, 4050
Weinberg, M. D. 1994, ApJ, 420, 597
Weinberg, M. D. 2024, arXiv:2403.12138
Weinberg, M. D., & Katz, N. 2007a, MNRAS, 375, 425
Weinberg, M. D., & Katz, N. 2007b, MNRAS, 375, 460
Weinberger, R., Springel, V., Hernquist, L., et al. 2017, MNRAS, 465, 3291
Weisz, D. R., Dolphin, A. E., Dalcanton, J. J., et al. 2011, ApJ, 743, 8
Wellons, S., Faucher-Giguère, C.-A., Hopkins, P. F., et al. 2023, MNRAS, 520, 5394
Wetzel, A., & Garrison-Kimmel, S., 2020a HaloAnalysis: Read and analyze halo catalogs and merger trees, Astrophysics Source Code Library, ascl:2002.014
Wetzel, A., & Garrison-Kimmel, S., 2020b GizmoAnalysis: Read and analyze Gizmo simulations, Astrophysics Source Code Library, ascl:2002.015
Wetzel, A., Hayward, C. C., Sanderson, R. E., et al. 2023, ApJS, 265, 44
Wetzel, A. R., Hopkins, P. F., Kim, J.-h., et al. 2016, ApJL, 827, L23
Xiang, K. M., Nataf, D. M., Athanassoula, E., et al. 2021, ApJ, 909, 125
Yu, S., Bullock, J. S., Klein, C., et al. 2021, MNRAS, 505, 889
Zana, T., Dotti, M., Capelo, P. R., et al. 2018a, MNRAS, 473, 2608
Zana, T., Dotti, M., Capelo, P. R., et al. 2018b, MNRAS, 479, 5214
Zhao, D., Du, M., Ho, L. C., Debattista, V. P., & Shi, J. 2020, ApJ, 904, 170